Manpreet Thesis

by Dr. Hem Dutt Joshi

Submission date: 27-Mar-2025 06:21PM (UTC+0530)
Submission ID: 2610337972
File name: Mthesis_without_ref.pdf (9.06M)
Word count: 20547
Character count: 104818

Performance Improvement of Generalized Frequency Division Multiplexing based 5G Communication System

A Thesis

Submitted in fulfillment of the requirement for the award of degree of
DOCTOR OF PHILOSOPHY

Submitted by
Manpreet Kaur
(Reg. No. 90176017)

Under the Guidance of
Dr. Hem Dutt Joshi
Senior Professor, ECED
Associate Professor

THAPAR INSTITUTE
OF ENGINEERING & TECHNOLOGY
(Deemed to be University)

Electronics and Communication Engineering Department
Thapar Institute of Engineering and Technology, Patiala, Punjab (India)
(Declared as Deemed-to-be-University u/s 3 of the UGC Act., 1956)

Chapter 1

Introduction

The modern wireless communication system has undergone significant advancements to meet the exponentially increasing demand for faster, ultra reliable, and ubiquitous connectivity. These networks support a wide range of services, from high-speed mobile internet to seamless device integration in the Internet of Things (IoT). With the advent of $5G$, emerging applications such as smart cities, autonomous vehicles, and augmented reality (AR) require efficient spectrum use, higher data rates, and minimal latency. To meet these requirements, the system must be both efficient and flexible. This efficiency can be enhanced through the use of versatile multicarrier modulation (MCM) schemes like Generalized Frequency Division Multiplexing (GFDM). GFDM's adaptability in time and frequency allocation, along with its pulse-shaping capabilities, makes it a highly suitable technique for advanced wireless communication systems [**?**].

This chapter presents an overview of the evolution of wireless communication systems and their current developments in Section 1.1. Section 1.2 discusses the architecture of $5G$ communication systems, followed by Section 1.3, which explores various $5G$ use cases. Section 1.4 highlights the advancements in next-generation communication systems. Section 1.5 presents the waveforms for $5G$ and beyond. Section 1.6 discusses the motivation for this work, while Section 1.7 provides an outline of the thesis organization.

1.1 Evolution of wireless communication system

The evolution of wireless communication systems has been remarkable, driven by technological advancements and the increasing demand for faster, more reliable, and efficient communication. Wireless communication refers to data transmission between devices or systems without physical cables or wires. It has become a crucial aspect of modern life, facilitating mobile communication, internet access, device remote control, and a wide range of other applications. The foundation of wireless communication was laid in the 19th century with the discovery of electromagnetic waves by James Clerk Maxwell in 1864 [**?**]. Later, in 1901, Guglielmo Marconi

was credited with building the first practical wireless telegraphy system, which he demonstrated with successful transatlantic radio communication [**?**]. In the early 20th century, radio became a widely used medium for entertainment, news, and communication. During World War II, around 1940, Bell Labs developed a system for secret telephony to fulfil the need for secure communications [**?**]. In 1948, the first fully automatic mobile telephone system for commercial use was set up in Richmond, Virginia, USA [**?**]. In the following years, the concept of cellular communication for commercial application was pioneered through the efforts of Bell Laboratories during the 1960s and 1970s.

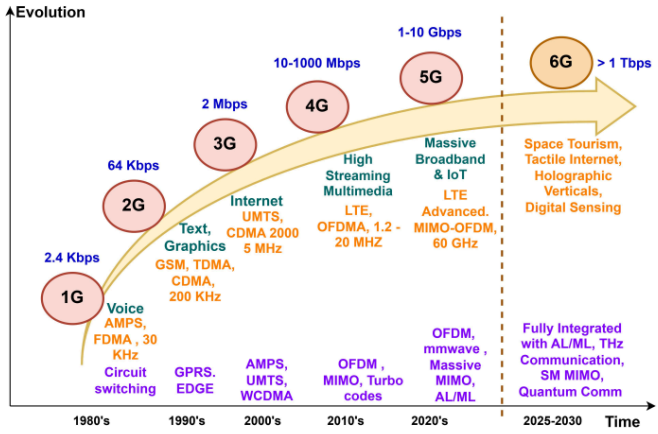

Figure 1.1: Wireless communication System from 1G to 6G.

The period from the early 1980s to the 1990s is referred to as the first generation ($1G$) of wireless communication, characterized by analog transmission. Systems within this generation offered voice calling exclusively, utilizing Frequency Division Multiple Access (FDMA). In 1990, second-generation ($2G$) mobile communication networks, utilizing digital modulation technologies, were introduced. The $2G$ network, based on the Global System for Mobile Communications (GSM), was designed to provide encrypted data services, such as Short Message Service (SMS), in addition to traditional voice communication [**?**]. Around the year 2000, third-generation ($3G$) mobile communication networks were introduced to address the increasing demand for a variety of multi-data services, such as video calls and internet browsing. The International Telecommunication Union (ITU) initiated the International Mobile Telecommunications (IMT-2000) program, leading to the creation of the $3G$ mobile standard utilizing Wideband Code Division Multiple Access (WCDMA) [**?**].

In 2009, the fourth generation ($4G$) of wireless communication, known as the Long-Term

Evolution (LTE) network, was introduced. This network offered expanded transmission bandwidth, high data rates, and broader mobile broadband connectivity through technologies such as Orthogonal Frequency Division Multiplexing (OFDM), Coordinated Multiple Transmission/Reception (CoMP), and Multiple-Input and Multiple-Output (MIMO) techniques. The arrival of the $5G$ era has brought network and service capabilities that were absent in previous generations [**?**]. The summary of all these mobile standards from 1G to 6G is given in Figure 1.1.

In 2017, the Third Generation Partnership Project (3GPP) introduced Release 15, the first 5G New Radio (NR) standard, to address the demands for unprecedented speeds, ultra-low latency, massive device connectivity, and exceptional network capacity [**?**]. The International Telecommunication Union (ITU-R) categorized 5G systems into three main use case scenarios: massive machine-type communications (mMTC), enhanced mobile broadband (eMBB), and ultra-reliable low-latency communications (URLLC) [**?**]. The main goal of $5G$ systems is to ensure uninterrupted connectivity ($10^6/km^2$ device density) with significantly higher data rates ($20Gbps$) and improved reliability, regardless of location or time [**?**].

1.2 5G Communication System

$5G$ operates across two primary frequency ranges: Sub-6 GHz Frequency Range 1 (FR1), spanning 450 MHz to 6 GHz, which provides wide coverage and reliable connectivity, and Millimeter Wave (mmWave, FR2), ranging from 24 GHz - 100 GHz, which enables ultra-high speed and low latency communication. $5G$ technology is comprised of two key components that collaborate to deliver high-speed with low-latency, and more reliable wireless communication:

- 5G NR – The Radio Access Network (RAN)
- 5G Core (5GC) – The Core Network

Each component plays an essential role in ensuring smooth connectivity, efficient data transmission, and effective network management. Below is a detailed breakdown of each component. Figure 1.2 presents the basic architecture of a $5G$ communication system.

1.2.1 5G New Radio

$5G$ NR is the wireless interface that connects user devices (UE) such as smartphones, IoT sensors, and autonomous vehicles to the $5G$ network. $5G$ NR serves as the global standard for mobile networks, offering significant advancements over previous generations like $4G$ LTE in terms of speed, capacity, latency, and flexibility. The journey towards $5G$ NR began with 3GPP Release 14, a key milestone that laid the groundwork for its development [**?**]. The $5G$ NR standard was officially introduced with 3GPP Release 15 (2017-2019), which focused on eMBB applications [**?**]. In 2020, 3GPP Release 16 ($5G$ Phase 2) was introduced, expanding

support for mMTC and URLLC. This release also enabled applications such as V2X (Vehicle-to-Everything) communication, Industrial IoT, and automation [**?**]. Next came 3GPP Release 17 in 2022, which optimized $5G$ for low-power, reduced-capability devices, enhancing its application in IoT. It introduced features like NR-Light, Satellite Integration, and expanded support for millimetre wave (mmWave) technology [**?**]. Looking ahead to 2024, 3GPP Release 18 marks the beginning of $5G$-Advanced, extending $5G$ capabilities beyond existing use cases. This release brings AI and machine learning-driven optimizations for network operations, resource management, and user experience. [**?**].

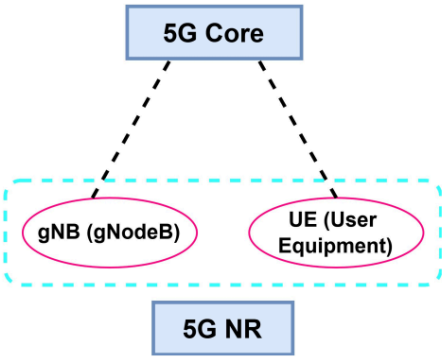

Figure 1.2: 5G Architecture [**?**]

1.2.2 5G Core

The $5G$ Core (5GC) is a cloud-native and service-based architecture (SBA) that manages network connections, data routing, authentication, and advanced network features like network slicing and edge computing. It replaces the traditional $4G$ LTE EPC (Evolved Packet Core) with a modular, virtualized, and software-driven approach, enabling seamless integration of emerging technologies like network slicing, edge computing, and AI-driven automation. The $5GC$ is built on network functions (NFs) that communicate via RESTful APIs, making it more dynamic and adaptable to different use cases. It features essential elements like the Access and Mobility Management Function (AMF) for handling user authentication and mobility, the Session Management Function (SMF) for overseeing session control, and the User Plane Function (UPF) for managing data routing. [**?**]. With enhanced security protocols, AI-driven traffic optimization, and cloud-native deployment, the $5G$ Core is the foundation for the future of ultra-fast, low-latency, and highly reliable communication networks.

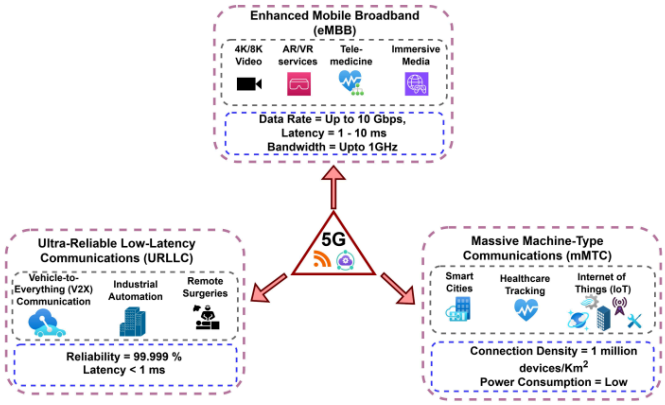

Figure 1.3: 5G Use Cases

1.3 5G Use cases

The International Telecommunication Union (ITU-R) has categorized 5G into three main usage scenarios under the IMT-2020 framework. These scenarios are designed to address different application needs and performance requirements. These applications focus on delivering ultra-fast data speeds, extremely low latency, large-scale connectivity, and more intelligent and efficient systems for both consumers and industries [**?**]. Figure 1.3 presents the requirements and applications of all use cases of the $5G$ communication system. These scenarios can be given as:

1. **Enhanced Mobile Broadband (eMBB):** According to IMT-2020, achieving ultra-low latency (1-10 ms) alongside high data rates (Up to 10 Gbps) is required and End-to-End Delay (E2E Delay) to be maintained within a few milliseconds. It focuses on increased capacity, and improved user experiences for applications that require fast and consistent mobile broadband services [**?**]. The eMBB involves consistent and periodic data streams, guaranteeing uninterrupted and time-sensitive communication, with data needing to be transmitted within defined time limits. Applications including smooth 4K/8K video streaming, augmented reality (AR), and the virtual reality (VR) experiences. The eMBB caters to bandwidth-intensive applications, including high-definition telepresence and telemedicine [**?**]. It also helps in Cloud-based VR gaming, virtual classrooms for remote learning and virtual concerts, live events, and 360-degree immersive experiences [**?**].

2. **Ultra-Reliable Low-Latency Communications (URLLC):** The second scenario, URLLC,

is designed to provide extremely low latency ($< 1ms$) and high reliability (99.999%) for wireless data transmission across both private and public cellular networks. It supports applications that demand near-instantaneous communication with exceptional reliability, making it essential for mission-critical tasks [**?**]. Key applications include autonomous driverless vehicles, automated industrial systems, smart grids, and remote surgeries with real-time feedback [**?**]. Vehicle-to-Everything (V2X) communication enables vehicles to interact with other vehicles, infrastructure, pedestrians, and surrounding elements, enhancing safety and transportation efficiency. It facilitates real-time communication between self-driving cars and their environment, ensuring safe navigation and collision avoidance. Additionally, it also plays a vital role in smart traffic monitoring and cooperative driving [**?**].

3. **Massive Machine-Type Communications (mMTC)** The mMTC scenario is built to accommodate a high density of connected devices, reaching up to 1 million per square kilometer. It prioritizes low power consumption and efficient transmission of small data packets, making it well-suited for IoT applications. It supports the rapid expansion of high-density IoT networks, including applications such as smart metering, smart infrastructure, healthcare tracking, and asset tracking [**?**]. $5G$ will enable massive IoT ecosystems with billions of devices connected in real-time, facilitating smart environments and automation. Applications of IoT include Smart Infrastructure and Logistics and Supply Chain which is based on real-time monitoring of infrastructure and goods and shipments [**?**].

1.4 Beyond 5G

The current $5G$ technology has brought a paradigm shift in the wireless communication systems, offering ultra high speeds, ultra-low latency, massive device connectivity, and remarkable network capacity. While $5G$ is still in its early stages of deployment and expansion, researchers and industry experts are already contemplating the requirements, challenges, and opportunities for "beyond $5G$"($B5G$) and $6G$ communication. The development of B5G is gaining attention as the global community seeks to redefine wireless communication systems for the future. The diverse requirements of the $B5G$ standards must administer data rates of 1 Gb/s, device density up to $10^7 devices/km^2$, high mobility ($1000km/h$) and latency of 10–$100\mu s$.

The future technologies for wireless communication come under $6G$ and are expected to be available by 2030. $6G$ technology aims to deliver an impressive data rate of 1 Tbps and achieve 100 percent global coverage by utilizing millimetre wave wireless communications and massive MIMO systems [**?**]. The first set of $6G$ technical specifications, known as Release 21, is expected to be finalized by 2026. This release will be part of the broader IMT-2030 framework. The trillions of connected industrial Internet of things (IoT), communication chan-

nels for vehicular-to-everything (V2X) and dense scene communications under global coverage scenarios impose the essential requirement to outperform the current wireless communication systems based on 5G NR [**?**].

1.5 Waveforms for 5G and B5G

Wireless and mobile traffic volume is projected to grow exponentially, increasing a thousand-fold within the next decade. with an estimated 50 billion devices connected to the cloud by 2025. These devices will require seamless data access and sharing anytime, anywhere. To meet these demands, next-generation waveforms for $5G$ are being explored. The physical layer waveform for 5G, especially within the NR standard, is engineered to accommodate a wide range of applications, from high-speed mobile broadband to URLLC. While $4G$ and $5G$ primarily rely on OFDM-based waveforms, Beyond $5G$ (B5G) is expected to adopt more advanced or hybrid waveform technologies, such as OFDM, FBMC, UFMC, and GFDM, to meet the advancing needs of future communication networks [**?**].

1. **Orthogonal Frequency Division Multiplexing (OFDM):** OFDM is a multi-carrier modulation (MCM) technique that splits a high-speed data stream into multiple low speed substreams, transmitting them simultaneously over orthogonal subcarriers. This enhances spectral efficiency, reduces inter-symbol interference (ISI), and improves resilience to multipath fading. OFDM offers high spectral efficiency by utilizing closely spaced orthogonal subcarriers, which minimize bandwidth wastage and enhance data transmission [**?**]. The OFDM signal in the time domain can be represented as

$$s(n) = \sum_{k=0}^{N-1} d_k \exp j2\pi k \frac{n}{N} \tag{1.1}$$

where, d_k is the complex data symbol modulated on the kth sub-carrier. The use of Fast Fourier Transform (FFT) ensures scalability and efficient modulation/demodulation processes. Additionally, OFDM is robust against narrowband interference, as data is spread across multiple subcarriers, minimizing the impact of frequency-selective fading. OFDM is widely used in $4G$ LTE, $5G$ NR, Wi-Fi (IEEE 802.11 a/g/n/ac/ax), Digital Video Broadcasting (DVB), and Ultra-Wideband (UWB) systems [**?**].

1. **Filter bank multicarrier (FBMC):** FBMC addresses the limitations of traditional OFDM and offers several advantages suited to the demanding requirements of future wireless networks. Unlike OFDM, FBMC eliminates the need for a CP, enabling more efficient bandwidth usage and enhancing spectral efficiency [**?**]. The baseband FBMC signal is

expressed as follows

$$S_{FBMC} = \sum_{-\infty}^{+\infty} \sum_{n=0}^{N-1} d_{m,n} g[k - m\frac{N}{2}] \exp j2\pi k \frac{n}{N} \exp j\phi^{m,n} \tag{1.2}$$

where represents the prototype filter, $\phi^{m,n}$ is an additional phase term at subcarrier n and symbol index m, which is expressed as $\frac{pi}{2}(m+n)$. In this expression, g denotes the prototype filter, and $\phi^{m,n}$ represents an extra phase term associated with subcarrier n and symbol index m, defined as $\frac{pi}{2}(m+n)$. The symbol $d_{m,n}$ is real-valued because the real and imaginary components are transmitted at different time instants. Additionally, to ensure the accurate reconstruction of received symbols, the prototype filter must adhere to the orthogonality condition. By using filter banks to shape the subcarriers, FBMC significantly reduces OOB emissions. Its individually filtered subcarriers also minimize ICI, providing better performance. Furthermore, FBMC demonstrates greater robustness against synchronization errors, including timing and frequency offsets, when compared with OFDM [**?**]. However, filtering operations for each subcarrier in FBMC are computationally more complex, and its integration with MIMO systems can be more challenging than with OFDM.

2. **Universal filtered multicarrier (UFMC):** Unlike OFDM, which relies solely on a cyclic prefix for protection without additional filtering, and FBMC, which applies filtering to individual subcarriers, UFMC filters groups of subcarriers, known as subbands. This method enables more efficient bandwidth utilization and significantly reduces out-of-band (OOB) emissions compared to OFDM. With a total of P subbands (blocks) and a filter of length F, UFMC signal is formulated as follows:

$$S_{UFMC} = \sum_{p=0}^{P-1} \sum_{f=0}^{F-1} \sum_{m=0}^{M-1} d_m^p g[l] \exp j2\pi k \frac{m-1}{M} \tag{1.3}$$

In this expression, d_m^p represents the complex data symbol transmitted on the m^{th} subcarrier within the p^{th} subband, while $g[l]$ denotes the represents the time-domain filter's frequency-equivalent windowing function. Similar to FBMC, UFMC eliminates the need for a cyclic prefix (CP), thereby reducing overhead and improving spectral efficiency. By applying filtering at the subband level, UFMC minimizes interference between adjacent subcarriers, further enhancing spectral efficiency [**?**]. The symbols are transmitted back-to-back without overlap, maintaining orthogonality in time. However, due to the absence of a CP, the symbols do not undergo circular convolution with the channel, requiring a more intricate receiver design. [**?**].

4. **Generalized Frequency Division Multiplexing (GFDM):** GFDM expands on the principles of OFDM but introduces key enhancements in flexibility and reduced OOB emis-

sions. Unlike OFDM, which transmits one subsymbol per subcarrier, GFDM is a multicarrier modulation technique that operates in blocks, with each block consisting of multiple subsymbols per subcarrier. This structure, combined with pulse-shaping on each subcarrier, significantly lowers OOB emissions, making GFDM more spectrally efficient. Considering P subcarriers in each subsymbol group and B subsymbol group in each block, a GFDM symbol is represented as follows:

$$S_{GFDM}[k] = \sum_{b=0}^{B-1} \sum_{p=0}^{P-1} d_{b,p} g_{b,p}[(k - bP) mod(BP)] \exp j2\pi k \frac{n}{N} \tag{1.4}$$

Here,$d_{m,p}$ represents the complex data symbol transmitted on the p^{th} subcarrier and the b^{th} subsymbol, while $g[n]$ denotes the prototype filter. As a versatile waveform, GFDM supports customizable subsymbols, subcarriers, and enhanced prototype filters to accommodate varying channel conditions and scenarios. Furthermore, the GFDM system is fully compatible with MIMO technology [**?**].

1.6 Motivation

The fast-paced evolution of present communication technologies has fueled the need for more efficient and flexible transmission methods capable of accommodating diverse applications. To meet the exponentially growing demands of $5G$ and future communication systems, it's essential to leverage advanced approaches such as appropriate physical layer waveforms, massive MIMO techniques, synchronization techniques, and millimeter-wave (mmWave) technologies. For this purpose, various waveforms, new channel model and synchronization techniques are proposed [**?**,**?**]. It is well-known that OFDM has been widely implemented as a key modulation scheme both in 4G and 5G standards due to its ability to effectively handle multipath channels and ease of implementation. However, OFDM is unable to effectively handle all challenges posed by different B5G scenarios because of its stringent synchronization requirements, significant extra load caused by CP, high PAPR and high levels of OOB emission. These challenges limit OFDM's suitability as the optimal waveform for next-generation networks [**?**].

GFDM is an advanced waveform well-suited for beyond 5G networks, offering key improvements over the widely used OFDM. GFDM's ability to transmit multiple subsymbols per subcarrier enables it to accommodate various applications, like high-speed data transmission, low-latency communication, and MTC. It is well-suited for dynamic environments like V2X or industrial IoT, where flexibility in frequency and time domains is crucial. Its ability to handle asynchronous transmissions and deliver low latency makes it well-suited for machine-to-machine ($M2M$) communications and Internet of Things (IoT) networks. GFDM's flexibility in allocating time and frequency resources positions it as an excellent choice for satellite-based broadband services, remote sensing, and defence communications. In vehicle-to-everything

($V2X$) communication systems, GFDM provides reduced latency and enhanced handling of Doppler shifts, crucial for high-speed vehicular networks. GFDM can be applied in wireless backhaul networks, offering high data rates and reliable connectivity, even in dense urban environments. Additionally, its low-latency properties make it ideal for multimedia applications such as real-time video streaming, online gaming, and augmented/virtual reality (AR/VR) [**?**].

Among the emerging waveforms, GFDM has garnered focus for its potential to improve error performance, spectral efficiency and resilience against various channel impairments. In the GFDM model, data is transmitted over multiple subcarriers, which can be adapted to meet specific system requirements. This flexibility allows for better handling of interference and more efficient utilization of available bandwidth, making it particularly suitable for next-generation communication standards, such as 5G and beyond. The GFDM system employs a unique filter design that reduces out-of-band emissions and enhances spectral efficiency, thereby facilitating the coexistence of multiple communication systems within the same frequency band. By analyzing the system model and operational characteristics of GFDM, we gain a deeper understanding of its role in advancing wireless communication technologies and overcoming the challenges of modern data transmission.

1.7 Thesis organization

The contents of the thesis are structured as follows.

Chapter 1 introduces the $5G$ wireless communication system, highlighting the current advancements in the field. It covers the requirements, applications, and key technologies of $5G$ systems, as well as the need for the GFDM system and its applications.

Chapter 2 provides an in-depth literature review of GFDM system and outlines the motivation behind this thesis. The latest research conducted by various scholars is discussed in chronological order, acknowledging their contributions to GFDM systems. The system model of GFDM is also presented in detail. Subsequently, the gaps identified in the existing studies are highlighted, and the objectives achieved in this work are elaborated.

Chapter 3 presents performance analysis of GFDM system. A closed-form expression for the ASER is formulated for GFDM systems operating over the FTR fading channel, considering imperfect channel estimation. Additionally, an asymptotic analysis of the GFDM system is also provided.

Chapter 4 introduces a novel timing synchronization technique for estimating the timing offset in GFDM systems, using a chirp signal as a training symbol. Performance of proposed timing synchronization technique is analyzed in both indoor office and urban macro (UMa) cell scenarios for the GFDM system.

Chapter 5 focuses on the design of a pulse-shaping filter for GFDM system, utilizing the discrete Gabor representation, the discrete biorthogonality conditions, and the Wigner distribution. Additionally, performance of the GFDM system is evaluated under various fading

conditions.

Finally, the main conclusions and future work are outlined in Chapter 6.

Chapter 2

GFDM system and its Analysis

A literature survey is essential before contributing to research in any field, as it presents an extensive analysis of previously published research in that area. This chapter presents a comparative literature survey on the GFDM systems, focusing on their development over time and performance analysis.

Section 2.1 provides a detailed explanation of the GFDM system model. A comprehensive review of GFDM performance analysis under various fading channels is provided in Section 2.2. The next section 2.3 presents a review about the available synchronization techniques for GFDM systems, while Section 2.4 presents an overview of the major filter design techniques for GFDM systems. Section 2.5 highlights the research gaps identified from the literature survey, while Section 2.6 summarizes the thesis objectives and outlines the scope of these objectives.

2.1 System model

GFDM is an innovative modulation scheme designed to enhance efficiency and flexibility of wireless communication systems. The GFDM system was first introduced in the year 2009 by Gerhard Fettweis *et al.* [**?**]. GFDM is a versatile MCM scheme, offering flexibility that enables it to encompass CP-OFDM ($M = 1$) and the single-carrier frequency domain equalization (SC-FDE) ($K = 1$) as specific cases [**?**]. The GFDM system model consist three main blocks: transmitter, channel, and receiver. The GFDM system considered in the present analysis is shown in Figure 2.1 and Figure 2.2 which depicts the schematic representations of the GFDM transmitter and modulator, respectively. The transmitter in this system employs a mapper that converts the input binary data into complex data symbol $\mathbf{d}_{k,m}$ using either μ-QAM or μ-PSK modulation technique. This serial complex data symbol is then given to the GFDM modulator, which processes the N-data symbol in parallel by decomposing it into K sub-carriers and M sub-symbols (i.e.$N = KM$). The $\mathbf{d}_{k,m}$ can be represented in terms of subsymbols (M) as follows

$$\mathbf{d} = [\mathbf{d}_0^T, \mathbf{d}_1^T, \mathbf{d}_2^T, \ldots, \mathbf{d}_{M-2}^T, \mathbf{d}_{M-1}^T]^T \tag{2.1}$$

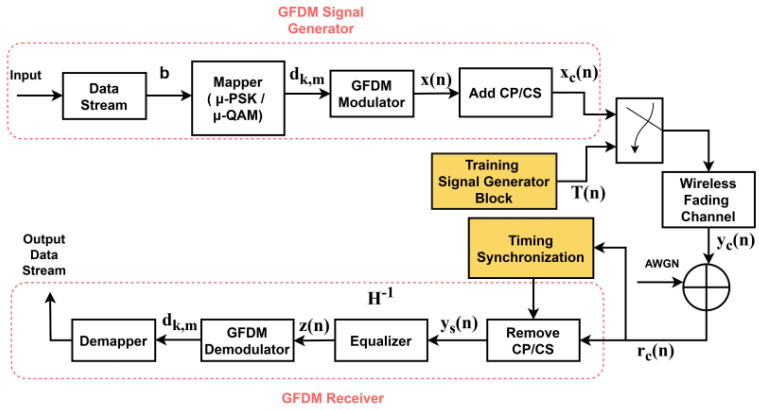

Figure 2.1: The System Model of GFDM

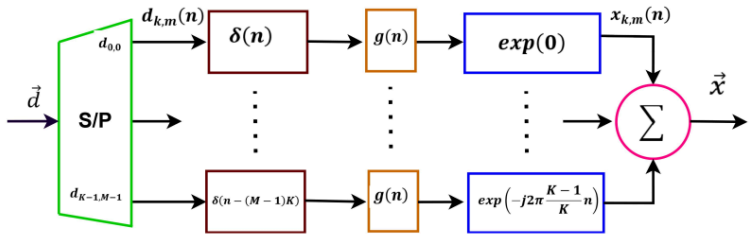

Figure 2.2: The GFDM Modulator

and it is represented in terms of subcarriers (K) as follows

$$\mathbf{d}_m = [d_{0,m}, d_{1,m}, , d_{2,m}, \ldots, d_{K-2,m}, d_{K-1,m}]^T \tag{2.2}$$

where $d_{k,m}$ represents the QAM symbol sent over the k^{th} subcarrier during the m^{th} subsymbol within the block. In the GFDM modulator, each $\mathbf{d}_{k,m}$ is transmitted using its corresponding pulse-shaping filter

$$\mathbf{g}_{k,m}[n] = g[(n - mk) \bmod N] \cdot \exp[-j2\pi kn/K] \tag{2.3}$$

Here, $\mathbf{g}[n]$ represents a user desired prototype discrete-time impulse response (generally RRC), with n as the sampling index. Each $\mathbf{g}_{k,m}[n]$ represents time- and frequency-shifted variant of $\mathbf{g}[n]$. The modulo operation ensures that $\mathbf{g}_{k,m}[n]$ is a circularly shifted form of $\mathbf{g}_{k,0}[n]$, while

the exponential introduces the shift in frequency. The transmitted symbol $\mathbf{x}[n]$ are generated by combining all transmitted samples

$$\mathrm{x}[n] = \sum_{k=0}^{K-1} \sum_{m=0}^{M-1} d_{k,m} g_{k,m}[n], \quad \text{for } n = 0, 1, ..., N-1 \tag{2.4}$$

Prototype filter samples in the vector form can be represented in form of

$$\mathbf{g}_{k,m}[n] = [g_{k,m}[0], g_{k,m}[1], g_{k,m}[2], \ldots, g_{k,m}[N-1]]^T \tag{2.5}$$

Based on the above representation of $\mathbf{g}_{k,m}[n]$, (2.4) can be given in matrix form

$$\mathbf{x} = \mathbf{A}\mathbf{d} \tag{2.6}$$

In the above expression the matrix $\mathbf{A}$ is a GFDM modulation matrix of dimensions $N \times N$ which is given in Figure 2.

$$\mathbf{A} = [\mathbf{g}_{0,0}, \cdots \mathbf{g}_{K-1,0} \quad \mathbf{g}_{0,1}, \cdots \mathbf{g}_{K-1,1} \quad \mathbf{g}_{0,M-1}, \cdots \mathbf{g}_{K-1,M-1}] \tag{2.7}$$

A CP is appended to the transmitting symbol $\mathbf{x}(n)$ to get the final symbol vector $\mathbf{x}_c(n)$. The modulated signal $\mathbf{x}_c(n)$ is then transmitted to a fading channel. On receiver end, assuming perfect synchronization and subsequent removal of the CP, the received signal may be presented as

$$\mathbf{y}_c = \mathbf{H}\mathbf{x}_c + \mathbf{w} \tag{2.8}$$

In this context, $\mathbf{H}$ represents the channel matrix, which takes the form of an $N \times N$ convolution matrix. The vector $\vec{w}$ corresponds to the noise, where each element signifies an independent and identically distributed (i.i.d) complex Gaussian random variable with a zero mean and variance σ^2. Assuming ideal channel estimation, channel equalization and demodulation is applied to received signal and it is represented by

$$\mathbf{z} = \mathbf{B}\mathbf{A}\mathbf{d} + \mathbf{B}\mathbf{H}^{-1}\mathbf{w} \tag{2.9}$$

In the above expression, $\mathbf{B}$ is a $N \times N$ receiver matrix. In GFDM system, several types of receivers are commonly used to demodulate the transmitted signal and mitigate inter-symbol and inter-carrier interference, which can arise due to the overlapping nature of subcarriers in GFDM. Here are some standard receiver options for GFDM:

- **Matched filter (MF) receiver** The MF receiver employs a filter that aligns with the transmitted pulse shape to maximize the signal-to-noise ratio for each subcarrier. The receiver matrix for the matched filter is defined as

$$\mathbf{B}_{MF} = \mathbf{A}^H \tag{2.10}$$

However, using a non-orthogonal transmit pulse may lead to self-interference.

- **Zero-forcing (ZF) receiver** The ZF receiver inverts the GFDM modulation matrix to eliminate interference. The receiver matrix for ZF is defined as

$$\mathbf{B}_Z F = \mathbf{A}^{-1} \tag{2.11}$$

While it removes both inter-symbol interference (ISI) and ICI, it can amplify noise, especially in channels with low signal-to-noise ratios (SNR).

- **Minimum mean square error (MMSE) receiver** The MMSE receiver reduces the MSE between the transmitted and received signals. The receiver matrix for MMSE receiver is defined as

$$\mathbf{B}_{MMSE} = (\mathbf{R}_w^2 + \mathbf{A}^H\mathbf{H}^H\mathbf{H}\mathbf{A})^{-1}\mathbf{A}^H\mathbf{H}^H \tag{2.12}$$

Here, $\mathbf{R}_w^2$ represents the noise covariance matrix. In MMSE reception, the channel is jointly equalized during the receiving process, eliminating the need for a zero-forcing channel equalizer block. This receiver balances between mitigating interference and controlling noise amplification.

2.2 Review of Performance analysis of GFDM

According to Barbara Minto, a former McKinsey consultant and author, "A well-crafted framework can act as both map and compass in the research process, leading researchers through uncharted territory with purpose". Minto's approach highlights that without a guiding structure, research risks becoming unfocused or overwhelming. A carefully developed framework keeps the research process intentional and coherent, making it easier to navigate complex relationships, draw meaningful insights, and communicate findings effectively [**?**].

The rapid evolution of communication systems is fueled by the demand for higher data rates, improved reliability, and efficient use of available spectrum. As modern applications expand into areas such as the Internet of Things (IoT), 5G, and emerging 6G technologies, communication systems must be robust enough to support diverse requirements, including low latency, high spectral efficiency, and resilience in various channel conditions. Performance analysis plays a critical role in assessing and optimizing the effectiveness of communication systems. Key performance metrics—such as symbol error rate (SER), spectral efficiency, SNR, and data throughput are used in evaluating system's reliability, efficiency, and capacity. By examining these metrics across different modulation schemes, channel models, and receiver

designs, researchers can gain insights into how various system parameters impact overall performance.

This subsection presents a review of selected published works on performance analysis of GFDM systems. To maintain clarity, the survey primarily focuses on performance analysis of GFDM system across different fading channels. Table 2.1 presents the survey on performance analysis of GFDM system.

In 2014, Nicola et al. analyzed the fundamental characteristics of the GFDM waveform, emphasized its key features, and derived analytical expressions for the SER in both additive white Gaussian noise (AWGN) and Rayleigh fading channels using a ZF receiver [**?**]. The exact analytical expressions for the SER of a ZR receiver-based GFDM system in Nakagami-m and Rician fading channels are formulated in [**?**]. Further, Ayhan *et al.* in 2016 formulated the expressions of SER for Maximal Ratio Transmission (MRT) based GFDM system under the same Nakagami-m fading conditions [**?**].In [**?**], analytical expressions for SER are derived for GFDM/OQAM under Rician fading channels and compared to conventional GFDM with QAM. The results show that GFDM/OQAM achieves improved SER performance compared to GFDM-QAM under similar channel conditions. [**?**] analyzes the SER performance of GFDM under various 3GPP-defined LTE fading profiles, including Extended Pedestrian Models (EPM), Extended Vehicular Models (EVM), and Extended Typical Urban Models (ETUM).

The performance of OQAM-GFDM based 5G wireless systems is analyzed for three channels: Highway Line-of-Sight (HLOS), Urban Approaching Line-of-Sight (UALOS), and Rural Line-of-Sight (RLOS). The GFDM/OQAM outperforms OFDM in all tested fading profiles, demonstrating better SER performance at lower Signal-to-Noise Ratios (SNRs) [**?**]. Approximate BER expressions are derived in [**?**] for Weighted-Type Fractional Fourier Transform (WFRFT) based GFDM over both AWGN and fading channels. Subsequently in 2018, the BEP for GFDM systems using an MMSE receiver over frequency-selective fading channels is analyzed for an M-QAM modulation scheme [**?**]. In 2019, Sapta *et al.* presented SER expressions for both standard QAM and offset QAM based GFDM systems with carrier frequency offset (CFO) over AWGN and TWDP channels [**?**]. Recently in 2022, Shravan *et al.* derived an expression for SER for GFDM in $\eta - \mu$ fading conditions for ZF receiver [**?**].

Table 2.1: Survey of Performance Analysis of GFDM systems

Year	**Baseband Modulation**	**Fading Channel**	**System Used**	**Performance Parameter**
2014 [**?**]	16 QAM	AWGN, Rayleigh	GFDM, MIMO-GFDM	SER
2015 [**?**]	4 QAM	Nakagami-m, Rician	GFDM	SER
2016 [**?**]	16 QAM	Nakagami-m	GFDM-MRT	SER
2016 [**?**]	OQAM	Rician-K	GFDM	SER
2016 [**?**]	QAM	Rayleigh, EPA, EVM, and ETUM	GFDM	PSD, SER
2017 [**?**]	OQAM	HLOS, UALOS, RLOS	GFDM	SER
2017 [**?**]	QPSK,16 QAM	ITU Vehicle, ITU Ped-B	WFRFT GFDM	BER, CCDF, PS
2018 [**?**]	QAM	frequency-selective fading	GFDM	CDF, BER
2019 [**?**]	BPSK, QPSK, QAM	AWGN, TWDP	GFDM	BER, SER
2022 [**?**]	16 QAM, 64 QAM	$\eta - \mu$	GFDM	SER
2022 [**?**]	QAM	Rayleigh, TWDP, Nakagami-q, Nakagami-m	STC-GFDM	ASER
2023 [**?**]	QAM	Rayleigh	FBMC, UFMC, GFDM	PAPR, PSD, SE, BER, SNR
2024 [**?**]	QAM	Rayleigh	DHT-GFDM, DHT-STC-GFDM	BER, AR

Further, in the same year, Surbhi *et al.* in [**?**] derived closed-form expressions for ASER of STC-GFDM systems under various fading conditions, including Rayleigh, TWDP, Nakagami-q, and Nakagami-m fading channels, specifically for μ-QAM. The study evaluates PAPR, PSD, SE, BER, and SNR for various multi-carrier modulation (MCM) schemes, including OFDM, FBMC, GFDM, and UFMC, in the context of 5G and future 6G networks. While OFDM is widely used for its simplicity, it faces challenges like high PAPR and significant out-of-band

emissions. FBMC achieves the lowest OOB emissions, and UFMC strikes a balance between spectral efficiency and PAPR performance. GFDM stands out by delivering superior PAPR reduction and BER performance across various fading scenarios [**?**]. In [**?**], advanced methods are presented to improve performance of GFDM systems by integrating Discrete Hartley Transform (DHT) and STC techniques, aiming to improve spectral efficiency, robustness, and reliability. The given methods are assessed based on spectral efficiency, complexity analysis, and bit error rate (BER) performance under Rayleigh fading channels using a ZF receiver.

2.3 Synchronization techniques

In GFDM, synchronization is essential because of the wave-form's non-orthogonal characteristics. and the unique pulse shaping used to reduce out-of-band emissions. Synchronization techniques in GFDM address timing and frequency offsets that can degrade system performance, especially in multipath fading and high-mobility environments like those in 5G and vehicular communications. The key synchronization techniques used in GFDM systems include timing synchronization, frequency synchronization, joint timing and frequency synchronization, pilot and preamble-based methods, blind synchronization, as well as matched filtering and correlation techniques. Effective synchronization techniques for GFDM enhance system performance by mitigating ISI and ICI, thereby enabling the efficient use of GFDM in applications requiring high data rates, low latency, and flexibility in carrier assignment. Synchronization remains a critical area of development in advancing GFDM's suitability for 5G and beyond.

Effective synchronization in GFDM is challenging but crucial to ensure the system's resilience to these errors. This section presents a review of selected published works on the synchronization techniques for GFDM systems. Table 2.2 presents several synchronization techniques present in the literature.

In 2014, Michailow *et al.* advanced the concept of GFDM by exploring its effectiveness across different fading channels and evaluating its performance using preamble-based synchronization techniques [**?**]. In the same year, Gaspar *et al.* introduced a data-aided synchronization scheme for estimating time and frequency offsets in GFDM. The effectiveness of the proposed technique was assessed based on synchronization accuracy and its influence on the SER in frequency-selective channels. [**?**].

[**?**] discusses an embedded midamble synchronization approach for GFDM systems, the focus is to achieve efficient time and frequency synchronization in GFDM by embedding a training sequence (midamble) within the payload, rather than using an isolated preamble. In 2015, [**?**] proposed a pseudo-circular preamble (PCP) embedded in the first subsymbol of GFDM symbols, this design integrates training and user data into a single block, aiming to improve synchronization and reduce overhead compared to traditional OFDM systems. Wang *et al.* evaluated a CP-based ML blind synchronization method for estimating the STO and CFO in GFDM systems in which an approximate-ML solution is discussed by simplifying the

covariance structure of GFDM signals, using an average signal power approximation [**?**].

Table 2.2: Survey of Synchronization Techniques for GFDM systems

Year	**Baseband Modulation**	**Fading Channel**	**Synchronization Technique**	**Performance Parameter**
2014 [**?**]	16 QAM	frequency-selective	Preamble, windowing	MSE, SER
2015 [**?**]	QAM	Rayleigh	Midamble	Mean, MSE
2015 [**?**]	QAM	Urban approach LOS, Street crossing NLOS, Highway LOS	Pseudo-Circular Preamble	MSE
2016 [**?**]	QAM	WSSUS	maximum-likelihood (ML) blind	MSE
2017 [**?**]	BPSK	AWGN	-	BER, ICI
2017 [**?**]	QPSK,64 QAM	Urban approach LOS, Highway LOS	Unique Word, Preamble	PSD, PER, Throughput
2018 [**?**]	16 QAM	Frequency selective	Pseudo-Noise Sequence	MSE, SER
2022 [**?**]	BPSK, QPSK, 16-PSK	Uma, Umi	Preamble	MSE, BER
2024 [**?**]	Equally likely Bernoulli	Rayleigh	CP based	RMSE
2024 [**?**]	QAM	AWGN, Dispersive channel	Preamble	MSE
2024 [**?**]	QAM	multipath fading	Windowed preamble	BER, MSE

An mathematical model is presented in [**?**] to assess BER performance degradation in GFDM systems when synchronization is imperfect. [**?**] focuses on developing synchronization, channel estimation, and equalization algorithms for the GFDM receiver, which are essential for accurate and reliable signal processing in dynamic vehicular environments. In [**?**], the authors propose a synchronization method utilizing a pseudo-noise (PN) sequence-based preamble consisting of two identical PN sequences, suitable for 5G systems. This PN-based synchronization demonstrates reduced mean squared error (MSE) and enhanced SER performance, even under challenging conditions involving significant STO or CFO values. Unlike traditional pilot-based techniques, the method proposed in [**?**] utilizes a preamble constructed from deterministic se-

quences (e.g., Zadoff-Chu sequences) to achieve both synchronization (STO and CFO) and channel equalization, resulting in improved frame efficiency. The approach was evaluated through simulations in urban macro (Uma) and urban micro (Umi) environments using various modulations, including BPSK, QPSK, and 16-PSK.

Recently in 2024, [**?**] proposed a joint synchronization method that estimates time and frequency offsets simultaneously by deriving a decision variable from the real part of an inner product. The effectiveness of the proposed technique is assessed for GFDM systems against existing synchronization methods in terms of the probability of perfect time synchronization, RMSE of offset estimates, and bit error ratio (BER). In the same year, [**?**] derived a generalized maximum likelihood estimation (MLE) algorithm for estimating frequency and time offsets in GFDM systems. This estimation is performed using a modified preamble that incorporates pulse shaping to enhance synchronization accuracy. The performance of the synchronization technique is analyzed over AWGN and multipath channel environments. In [**?**], symbol timing estimation, frequency offset estimation, and the channel estimation algorithms are utilized to assess GFDM performance in frequency-selective channels. The preamble design incorporates multiple identical segments, facilitating a wider frequency estimation range while increasing complexity.

2.4 Filter design techniques

Filter design is a cornerstone of GFDM's adaptability and efficiency in modern communication systems. Techniques range from simple raised cosine filters to advanced time-frequency optimized designs, each tailored to specific performance requirements. The inherent non-orthogonality of GFDM requires filters that effectively minimize interference while preserving system flexibility. However, high-performance filters can introduce greater computational complexity and latency, posing challenges for real-time implementation. Additionally, filters must be adaptable to varying bandwidths and carrier configurations in diverse 5G environments. Effective filter design enables GFDM systems to fulfill the requirements of future wireless systems, including high spectral efficiency, minimal latency, and robust interference management.

Filter design for GFDM requires careful consideration to meet these objectives while adapting to the unique block-based structure of GFDM symbols, which contain multiple subcarriers and subsymbols. This section provides a review of selected published works on filter design techniques for GFDM systems. Table 2.3 presents various filter design techniques for the GFDM system.

In 2016, Seungyul Han et al. introduced an optimal filter-designing technique based on rate maximization and OOB radiation minimization. Their study presented a trade-off analysis between transmission rate and OOB radiation for GFDM systems. Additionally, the research addressed OOB emission reduction and proposed a joint design framework for filters and windowing to balance spectral efficiency and performance [**?**]. Further, in 2017 [**?**] investigated

the use of "Better than Nyquist" pulse-shaping filters, including Xia pulses, root ramp filters, and other Nyquist-enhanced designs, to improve the SER performance of GFDM systems. The study focuses on scenarios with a ZF receiver operating in an AWGN channel using 16-QAM modulation. The study in [?] introduces a filter optimization algorithm aimed at minimizing OOB radiation while preserving strong in-band performance metrics, including MSE and SER. The above optimization algorithm is framed as a non-convex problem leveraging the characteristic matrix of the GFDM transmitter.

Table 2.3: Survey of Filter Design Techniques for GFDM systems

Year	**Baseband Modulation**	**Fading Channel**	**Filter Used**	**Performance Parameter**
2016 [?]	-	AWGN , LTE Pedestrian B	Optimized Filter	PSD, Transmission rate
2017 [?]	16 QAM	AWGN	RRC, Fsech, Farcsech	SER
2017 [?]	QPSK	AWGN	characteristic matrix based filter	PSD, SER
2019 [?]	16 QAM	AWGN	Linear combination of two pulses	SEP
2019 [?]	16 QAM	Rayleigh	Quadratic programming based filter	PSD, PAPR, BER
2019 [?]	QPSK	HIPERLAN/2 Channel A	Optimized Filter	BER, PAPR
2020 [?]	16 QAM	HIPERLAN/2 Class A	Quadratic programming based filter	PSD, BER, EE
2022 [?]	BPSK, MQAM	AWGN	Optimized Nyquist pulse	PSD, BER
2023 [?]	4 QAM	AWGN	Genetic Algorithm based Filter	BER
2024 [?]	PSK, QAM	AWGN, Multipath fading	Optimized Filter	PSD, BER

In [?], a new pulse-shaping filter for GFDM systems is proposed, designed as a linear com-

bination of two pulses. The filter exhibits enhanced vertical and horizontal sharpness in the eye diagram compared to the RRC filter, indicating improved tolerance to ISI. The filter performance is analyzed for 16 QAM over an AWGN fading using ZF, MF, and MMSE receivers. In 2019, Sim *et al.* proposed a practical pulse-shaping filter for GFDM systems based on quadratic programming. The design optimizes the frequency response to minimize stopband energy while adhering to passband constraints, thereby reducing OOB radiation and maintaining performance in terms of PAPR and BER [**?**]. Moreover, [**?**] also utilized a quadratic programming approach to develop a pulse-shaping filter for GFDM, specifically targeting minimization of PAPR, which directly impacts power efficiency and contributes to non-linear distortions in the high power amplifier (HPA). The proposed filter demonstrated improved PAPR performance, while maintaining error performance comparable to that of the RRC filter.

Using the same QP approach, [**?**] designed a pulse-shaping filter to reduce OOB radiation in GFDM systems while ensuring acceptable in-band performance metrics, including BER and PAPR. In [**?**], an optimized finite-length Nyquist filter is proposed, incorporating constraints such as energy limitations, zero-crossing conditions, boundary conditions for derivatives, and a novel parameter called Spectral Density Energy Concentration Degree (SDECD). The filter demonstrates superior performance in suppressing OOBR compared to traditional Nyquist pulses.In [**?**], a novel approach is proposed for optimizing pulse-shaping filters in GFDM systems using a Genetic Algorithm (GA). The algorithm iteratively searches for optimal filter parameters that minimize BER while preserving the general characteristics of standard pulse-shaping filters. In [**?**], presents an innovative framework and mathematical model to analyze and mitigate self-interference in GFDM. The study decomposes self-interference into two orthogonal components using a vectorized representation, providing a deeper theoretical understanding. It derives analytical expressions for self-interference based on prototype filter parameters in the frequency domain, leading to the proposal of an optimal filter design strategy.

2.5 Research Gaps

The following gaps are observed from the literature study:

- GFDM has emerged as a leading waveform candidate for the air interface in 5G communications. Performance analysis of GFDM systems has been conducted for various channel models, including AWGN [**?**], Rayleigh [**?**, **?**], Nakagami-m [**?**], Nakagami-q [**?**], Rician [**?**], TWDP [**?**], and $\eta - \mu$ [**?**] channels, using modulation schemes such as QAM, offset QAM, and PSK. Additionally, the analysis of GFDM performance under recently introduced fading environments like $k - \mu$ [**?**], $\alpha - \mu$ [**?**], Generalized-K [**?**] and FTR [**?**] fading presents significant potential for further research.

- GFDM systems experience significant performance degradation without proper synchronization, leading to higher error rates, reduced throughput, and increased interference,

highlighting the necessity of synchronization for practical deployment. Research in this area has explored various synchronization techniques for GFDM communication systems utilizing methods such as unique word [?], preamble based [?, ?, ?, ?, ?], CP based, midamble based [?] and maximum likelihood blind [?] synchronization. Future studies could propose novel synchronization approaches by addressing timing offset and carrier frequency offset for GFDM in diverse fading channel conditions.

- Filter design is a crucial component of GFDM, enabling the optimization of signal quality, interference reduction, and adaptability to diverse 5G and beyond communication scenarios. From the literature survey, it is evident that various approaches have been employed for filter design, including the characteristic matrix method [?], quadratic programming (QP) [?, ?], the application of nyquist pulses [?, ?], Genetic Algorithm [?] and the combination of different pulse shapes [?]. In the future, various approaches can be proposed for designing prototype filters to enhance the performance of GFDM systems.

2.6 Thesis Objective and Scope

30

In this chapter, the SER of the GFDM system is evaluated using both exact closed-form expressions and asymptotic analysis. The analysis assumes a fluctuating two-ray (FTR) fading scenario to derive the exact asymptotic error rate expressions. Additionally, the evaluation is conducted for μ-QAM modulation scheme under conditions of imperfect channel estimation.

Numerical simulations of derived expressions have been used to assess performance of the GFDM across different channel conditions and system parameters. Simulation results are presented alongside numerical calculations, and they are found to closely match the numerical results. The derived ASER expressions can be used as a foundation for calculating performance of the GFDM under various fading scenarios, including TWDP, Rayleigh, and Nakagami fading.

This dissertation aims to enhance performance of GFDM system by first analyzing its existing performance and then introducing improvements through a proposed synchronization technique and pulse-shaping filter design:

- To analyze the performance of GFDM based 5G communication system under the effect of different fading channels.
- To design an efficient synchronization technique for GFDM based 5G communication system.
- To improve the performance of GFDM based 5G communication system by interference mitigation.

This dissertation examines performance of the GFDM system across various fading environments. Precise closed-form and asymptotic expressions for the error rate are derived. Additionally, the impact of channel impairments, such as imperfect CSI, on the ASER is evaluated to assess GFDM system performance.

The second objective focuses on developing an efficient synchronization method for GFDM. A novel timing synchronization algorithm that combines cross-correlation with a sliding window approach. The algorithm leverages a training symbol constructed using a chirp sequence. Its performance is assessed across diverse fading environments, such as indoor office and urban macrocell scenarios, using metrics like mean, mean squared error (MSE), and timing failure probability.

The third objective aims to improve the performance of GFDM based 5G communication systems by interference mitigation. A pulse-shaping filter is developed using discrete Gabor representation, discrete biorthogonality conditions, and Wigner distribution. The GFDM system's performance is assessed using parameters like out-of-band (OOB) radiation and SER across various channel conditions, including AWGN, Rayleigh, Nakagami-m, TWDP, and Nakagami-q fading channels.

Chapter 3

Performance Analysis of GFDM over Different Fading Channels

The performance of GFDM system in terms of SER is evaluated using both exact and closed-form analysis. The FTR fading model is utilized to derive exact error rate expressions, enabling the calculation of the ASER for GFDM systems under various fading scenarios, including one-sided Gaussian, Rayleigh, Rician, Hoyt, Nakagami, and TWDP as its special cases. An asymptotic error rate is also derived alongside the exact expressions, with the analysis specifically conducted for MQAM modulation techniques.

Numerical simulations of the derived expressions have been utilized to evaluate the performance over various parameters of GFDM and fading channel. Simulation results are shown alongside numerical results, demonstrating close agreement.Since obtaining perfect CSI at the receiver is typically unrealistic in practical scenarios, this chapter examines how imperfect CSI affects the ASER performance of the GFDM system.

The error rate analysis over the fluctuating two-ray (FTR) fading channel is presented in Section 3.1, where the exact and asymptotic expressions for ASER of GFDM system are formulated. Section 3.2 discusses the results obtained from numerical analysis and Monte Carlo simulations, while the section 3.3 concludes the chapter by providing a summary.

3.1 Symbol Error Rate Analysis

The GFDM system's error rate performance is influenced by three key factors: modulation technique, fading channel, and system impairments. First, it is crucial to characterize the fading channel using appropriate models such as Rayleigh, Rician, Nakagami-m, or fluctuating two-ray (FTR). Second, the impact of channel impairments, including timing offsets, carrier frequency offsets (CFO), and imperfect CSI, is incorporated into the error rate calculations. Finally, the symbol error rate (SER) is derived using modulation schemes like MQAM or MPSK, based on the fading probability density function (PDF) and channel statistics.

In this analysis, the ASER is generally obtained by integrating the conditional SER $P(e/\gamma)$ and fading channel PDF from 0 to ∞. Next, the conditional error rate is utilized to formulate the expression for the error rate $P(e)$ in the AWGN fading for GFDM. Additionally, a simple exponential bound for the conditional error rate is provided. Finally, closed-form expressions for ASER of GFDM over diverse fading channels are derived using these conditional error rates. In the present analysis, the μ-QAM modulation is considered to evaluate the SER analysis for the FTR fading channel.

Consider the modulated signal $\vec{x}_c$ being transmitted over a wireless fading channel. Under the assumption of perfect synchronization and after CP removal, the received signal is represented as

$$\vec{y} = \mathbf{H}\vec{x} + \vec{w} \tag{3.1}$$

where, $\mathbf{H}$ is a $N \times N$ channel matrix (circulant) with impulse response $\vec{h}$ $(= [h_0, h_1, , h_2..., h_{L-1}]^T)$ with zero padding as its column vector and L represents number of channel taps. The vector $\vec{w} \sim \mathcal{CN}(0, {\varrho_w}^2 \mathbf{I}_N)$ denotes AWGN with mean zero and ${\varrho_w}^2$ variance. Assuming both $\mathbf{H}$ and $\vec{w}$ are ergodic and stationary with each of their entries being independent, identically distributed (i.i.d.) and zero-mean circularly symmetric complex Gaussian (ZMCSCG).

At the receiver, a MMSE channel estimation is considered. The channel estimation error ($\mathbf{A}$) is given as

$$\mathbf{A} = \mathbf{H} - \tilde{\mathbf{H}} \tag{3.2}$$

where, $\tilde{\mathbf{H}}$ is channel response estimation. According to MMSE estimation property, $\tilde{\mathbf{H}}$ and $\mathbf{A}$ are uncorrelated, with the elements of $\mathbf{A}$ following a ZMCSCG distribution with ${\varrho_A}^2$ variance. The entries of $\tilde{\mathbf{H}}$ are also i.i.d. ZMCSCG with variance $(1 - {\varrho_A}^2)$. By using the property of MMSE, the variance of $\mathbf{A}$ is determined as

$${\varrho_A}^2 = \varepsilon\left(|\boldsymbol{\rho}|^2\right) - \varepsilon\left(|\tilde{\boldsymbol{\rho}}|^2\right) \tag{3.3}$$

The parameter ${\varrho_A}^2$ quantifies the accuracy of channel estimation. It is presumed that the value of ${\varrho_A}^2$ is known to both the transmitter and receiver. The instantaneous SNR (γ_t) of GFDM for frequency-selective fading channels under imperfect CSI at the receiver can be given as

$$\gamma_t = \frac{\gamma}{1 + {\varrho_A}^2 \gamma}, \tag{3.4}$$

where

$$\gamma = \frac{3R_T}{2(2^\mu - 1)} \frac{E_s}{\xi N_o}, \tag{3.5}$$

and

$$R_T = \frac{KM}{KM + N_{cp} + N_{cs}}. \tag{3.6}$$

where, The parameter ξ represents the noise enhancement factor (NEF), μ is the modulation

order of QAM, $p = \sqrt{2^{\mu}}$, K signifies the total number of subcarriers, and M indicates the number of subsymbols within the GFDM system. N_{cp} and N_{cs} represent the lengths of the CP and cyclic suffix (CS), respectively, Additionally, E_s denotes the average energy per symbol, while N_o corresponds to the noise power spectral density. Now, the ASER ($P_t(e)$) of GFDM in terms of γ_t is expressed as

$$P_t(e) = \int_0^{\infty} P_t(e/\gamma_t) f_{\gamma_t}(\gamma_t) d\gamma_t, \tag{3.7}$$

where, $f_{\gamma_t}(\gamma_t)$ is PDF of the fading channel, and $P(e/\gamma_t)$ is the conditional ASER of the μ-QAM modulation over AWGN channel which is given as [**?**].

$$P_t(e/\gamma_t) = 2\left(\frac{p-1}{p}\right)\text{erfc}(\sqrt{\gamma_t}) - \left(\frac{p-1}{p}\right)(\text{erfc})^2(\sqrt{\gamma_t}). \tag{3.8}$$

The ASER for the GFDM across various fading channels can be determined using the following expression

$$ASER_{exact} = \int_0^{\infty} 2\left(\frac{p-1}{p}\right)\text{erfc}(\sqrt{\gamma_t}) f_{\gamma_t}(\gamma_t) d\gamma_t - \int_0^{\infty} \left(\frac{p-1}{p}\right)\text{erfc}^2(\sqrt{\gamma_t}) f_{\gamma_t}(\gamma_t) d\gamma_t, \tag{3.9}$$

The ASER performance of GFDM can be determined by evaluating the above integral with the respective channel PDF. Various approaches can be employed to evaluate the error performance analysis of a communication system, including exact, moment-generating function (MGF)-based, approximate, and asymptotic approaches. In our work we have used

- Exact analysis
- Asymptotic analysis

The ASER expression for GFDM systems has been derived for various channel models, including AWGN [**?**], Rayleigh [**?**], Nakagami-m [**?**], Nakagami-q [**?**], Rician [**?**], TWDP [**?**], and $\eta - \mu$ [**?**] channels. However, in this work, we consider a more generalized channel model, namely the fluctuating two-ray (FTR) channel. The PDFs of the one-sided Gaussian, Rayleigh, Rician, Hoyt, Nakagami, and TWDP fading models are special cases of the FTR distribution. Table 3.1 illustrates the relationship between the FTR fading channel and various fading models discussed in the literature. The recently proposed fluctuating two-ray (FTR) fading model is better suited for capturing the characteristics of small-scale fading in outdoor mm-wave channels operating at 28 GHz [**?**]. In the year 2017, Romero-Jerez *et al.* introduced the FTR fading model [**?**], which was subsequently improved in 2021 by M. Lopez-Benitez *et al.* [**?**]. The FTR fading channel consists of two fluctuating specular components with random phases and a diffuse component. The complex baseband response of the FTR channel can be represented

as

$$C_r = \sqrt{\varsigma} C_1 \exp(i\theta_1) + \sqrt{\varsigma} C_2 \exp(i\theta_2) + X + iY \tag{3.10}$$

where C_1 and C_2 represent fixed amplitudes associated with specular components influenced by a Nakagami-m random variable, while θ_1 and θ_2 are random phases uniformly distributed within the interval $[0, 2\pi)$. The random phase of each dominant component is considered statistically independent. Furthermore, $X + iY$ represents the diffuse component, modeled as a complex Gaussian random variable, where both X and Y follow a normal distribution with mean 0 and variance σ^2. ς denotes the Gamma-distributed random variable with a mean one, and the PDF of ς can be formulated as follows:

$$f_\varsigma(u) = \frac{m^m u^{m-1}}{\gamma(m)} e^{-mu} \tag{3.11}$$

where u represents potential realizations of the random variable, parameter m determines degree of fading in channel, and the value of m must be a positive real number that can take any arbitrary value. The fading envelope has FTR statistics, and the PDF representing instantaneous SNR γ per symbol is given as [**?**]

$$f_\gamma(\gamma) = \frac{m^m}{\Gamma(m)} \sum_{r=0}^{\infty} \frac{K_f^r d_r}{r!} f_G(\gamma; r+1, 2\sigma^2) \tag{3.12}$$

where

$$f_G(\gamma; r+1, 2\sigma^2) = \frac{\gamma^r}{\Gamma(r+1)(2\sigma^2)^{(r+1)}} \exp\Big(-\frac{\gamma}{2\sigma^2}\Big) \tag{3.13}$$

and the coefficient d_r is given by

$$\begin{aligned} d_r = \sum_{s=0}^{r} \binom{r}{s} \sum_{l=0}^{s} \binom{s}{l} \Gamma(r+2l+m-s)\ (m+K_f)^{-(r+2l+m-s)} \\ \times\ K_f^{2l-s} \Big(\frac{\Delta}{2}\Big)^{2l} (-1)^{2l-s}\ R_{r+m}^{s-2l}\Big([K_f\Delta/(m+K_f)]^2\Big). \end{aligned} \tag{3.14}$$

Here, $2\sigma^2 = \bar{\gamma}/(1+K_f)$ where $\bar{\gamma}$ is the average SNR at the GFDM receiver, $K_f = \frac{{C_1}^2+{C_2}^2}{2\sigma^2}$ is defined as the relative power between the dominant and reflected signals, and $\Delta = \frac{2C_1C_2}{{C_1}^2+{C_2}^2} \in [0, 1]$ is used to indicate the degree of similarity between the two primary waves. The function $R_v^\eta(x)$ in (3.14) is defined in [**?**] as

$$R_v^\eta(x) = \begin{cases} \big(\frac{v-\eta}{2}\big)_\eta \big(\frac{v-\eta+1}{2}\big)_\eta \frac{x^\eta}{\eta!}\ {}_2F_1\Big(\frac{v+\eta}{2}, \frac{v+\eta+1}{2}; 1+\eta; x\Big), & \eta \in N^+ \\ {}_2F_1\big(\frac{v-\eta}{2}, \frac{v-\eta+1}{2}; 1-\eta; x\big)/(\Gamma(1-\eta)), & \text{otherwise} \end{cases} \tag{3.15}$$

where, $(p)_a = \Gamma(p+a)/\Gamma(p)$ is Pochhammer symbol, and ${}_2F_1$(u, v; w; x) is Gauss hypergeometric function. In the FTR model, the constant amplitude of specular waves experiences

random fluctuations. This stochastic nature enables a more accurate representation of the signal's amplitude variations compared to the TWDP model, which is specific case included within the FTR model [**?**].

Table 3.1: Connection between FTR Fading Channel and Diverse Fading Channels in Literature [**?**]

Channels	**FTR Channel Parameters**
Rayleigh	$\Delta = 0, K_f \to \infty, m_f = 1$
One-Sided Gaussian	$\Delta = 0, K_f \to \infty, m_f = 0.5$
Nakagami-m	$\Delta = 0, K_f \to \infty, m_f = m_f$
Hoyt	$\Delta = 0, K_f = \frac{1-q^2}{2q^2}, m_f = 0.5$
Rician	$\Delta = 0, K_f = K_f, m_f \to \infty$
TWDP	$\Delta = \Delta, K = K_f, m_f \to \infty$
Two-Wave	$\Delta = \Delta, K_f \to \infty, m_f \to \infty$
Fluctuating Two-Wave	$\Delta = \Delta, K_f \to \infty, m_f = m_f$

3.1.1 ASER using Exact Analysis

Since our study focuses on the FTR fading channel, the exact closed-form ASER expression for GFDM over this channel can be obtained by substituting the PDF of the FTR fading into the given equation

$$ASER_{exact} = R_0 \int_0^{\infty} (1 - erf(\sqrt{\gamma_t})) \left(\sum_{r=0}^{\infty} f_G(\gamma; r+1, \frac{\bar{\gamma}_t}{(1+K_f)} \right) d\gamma - \frac{R_0}{2} \int_0^{\infty} erfc^2(\sqrt{\gamma_t}) \left(\sum_{r=0}^{\infty} f_G(\gamma; r+1, \frac{\bar{\gamma}_t}{(1+K_f)} \right) d\gamma, \tag{3.16}$$

where

$$R_0 = 2 \left(\frac{p-1}{p} \right) \frac{m^m}{\Gamma(m)} \sum_{r=0}^{\infty} \frac{K_f^r d_r}{r!} \tag{3.17}$$

Rewriting the above equation we get

$$ASER_{exact} = S_1 - S_2, \tag{3.18}$$

To derive the exact closed-form expression for ASER, the integrals S_1 and S_2 must be evaluated. Substitute (3.13) in (3.16) and further solving S_1 by substituting the value of $f_G(\gamma_t; r+1, 2\sigma^2)$

we get

$$S1 = R_0 \int_0^\infty (1 - erf(\sqrt{\gamma_t})) \left(\frac{\gamma_t^r (K_f + 1)^{(1+r)}}{\Gamma(r+1)\bar{\gamma}_t^{(1+r)}} \exp\Big(- \frac{\gamma_t (1 + K_f)}{\bar{\gamma}_t} \Big) \right) d\gamma \tag{3.19}$$

Now, (3.19) can be further simplified as

$$S_1 = R_0^{'} \int_0^\infty (1 - \text{erf}(\sqrt{\gamma_t})) \gamma_t^r \exp\Big(- \frac{\gamma_t (1 + K_f)}{\bar{\gamma}_t} \Big) d\gamma_t, \tag{3.20}$$

where

$$R_0^{'} = \frac{R_0 (1 + K_f)^{(1+r)}}{\Gamma(1+r)\bar{\gamma}_t^{(1+r)}}, \tag{3.21}$$

Now further solving the integral in (3.20) by using [**?**], Eq. (6.286), and Eq. (8.250), S_1 is expressed as

$$S_1 = \frac{R_0^{'} \Gamma(r+1)}{(2r+1)\sqrt{\pi}} \times {}_2F_1\left(r + \frac{1}{2}, r + 1; r + \frac{3}{2}; \left(\frac{-(1 + K_f)}{\bar{\gamma}_t} \right) \right), \tag{3.22}$$

In the above expression, ${}_2F_1(a, b; c; z)$ is the Gauss hypergeometric function [**?**], Eq. (9.14.1-2). Next, solving S_2 by substituting the value of $f_G(\gamma_t; r + 1, 2\sigma^2)$ from (3.13) we get

$$S2 = \frac{R_0}{2} \int_0^\infty erfc^2(\sqrt{\gamma_t}) \left(\sum_{r=0}^{\infty} \left(\frac{\gamma_t^r (K_f + 1)^{(1+r)}}{\Gamma(1+r)\bar{\gamma}_t^{(1+r)}} \exp\Big(- \frac{\gamma_t (1 + K_f)}{\bar{\gamma}_t} \Big) \right) \right) d\gamma \tag{3.23}$$

Further solving above equation (3.23)

$$S_2 = \frac{R_0^{'}}{2} \int_0^\infty \text{erfc}^2(\sqrt{\gamma_t}) \gamma_t^r \exp\Big(- \frac{\gamma_t (1 + K_f)}{\bar{\gamma}_t} \Big) d\gamma_t, \tag{3.24}$$

The expression of S_2 can be solved using integration by parts, with $u = \text{erfc}^2(\sqrt{\gamma_t})$ and $dv = \gamma_t^r \exp\Big(- \frac{\gamma_t (1+K_f)}{\bar{\gamma}_t} \Big)$. After solving the integral in (3.24) , S_2 can be written as

$$S_2 = \frac{R_0}{2} \left(1 - \frac{4R_1}{\sqrt{\pi}} \int_0^\infty (1 - \text{erf}(\sqrt{\gamma_t})) \sqrt{\gamma_t}^{2i} \exp\Big(- \gamma_t \Big(\frac{(1 + K_f)}{\bar{\gamma}_t} + 1 \Big) \Big) \right) d\gamma_t, \tag{3.25}$$

where,

$$R_1 = \frac{\sum_{i=0}^{r} (1 + K_f)^i}{((i!)\bar{\gamma}_t{}^i)} \tag{3.26}$$

The above expression in (3.25) can be further simplified using [**?**], Eq. (6.286), and Eq. (8.250),

$$S_2 = \frac{R_0}{2} \left(1 - \frac{4}{\pi} \sum_{i=0}^{r} \frac{(1 + K_f)^i}{\bar{\gamma}_t{}^i (2i+1)} \times {}_2F_1\left(i + \frac{1}{2}, i + 1; i + \frac{3}{2}; \left(\frac{-(1 + K_f)}{\bar{\gamma}_t} - 1 \right) \right) \right), \tag{3.27}$$

The closed form expression of ASER for the GFDM under FTR fading channel can be obtained by putting equations (3.22) and (3.27) in (3.18) and can be written as

$$ASER_{exact} = \frac{R_0'\Gamma(r+1)}{(2r+1)\sqrt{\pi}} \times {}_2F_1\Big(\frac{1}{2}+r, 1+r; \frac{3}{2}+r; \frac{-(1+K_f)}{\bar{\gamma}_t}\Big) - \frac{R_0}{2}\Big(1 - \frac{4}{\pi}\sum_{i=0}^{r}\frac{(1+K_f)^i}{\bar{\gamma}_t{}^i(2i+1)} \times {}_2F_1\Big(\frac{1}{2}+i, 1+i; \frac{3}{2}+i; \frac{-(1+K_f)}{\bar{\gamma}_t} - 1\Big)\Big). \tag{3.28}$$

3.1.2 ASER using Asymptotic Analysis

Asymptotic analysis in communication systems focuses on evaluating system performance at extreme conditions, such as very high SNR. The basic concept behind asymptotic analysis is to evaluate the behavior of a system or mathematical function under extreme conditions, typically as an input parameter approaches a limit, such as infinity or zero. For GFDM, asymptotic analysis is particularly useful for identifying the error rate floor, dominant system impairments, or key design parameters that impact performance under fading conditions. This approach aids in simplifying performance evaluation and guiding system optimization. For asymptotic analysis, the higher values of average SNR are considered, due to which $2\sigma^2$ approaches infinity.

Asymptotic PDF

The term corresponding to $r = 0$ holds the maximum value, and by removing the remaining terms from the expression of d_r in (3.14), the coefficient d_0 can be obtained as

$$d_0 = \Gamma(m)(m+K_f)^{-m} R_m\Big(\Big[\frac{K_f\Delta}{m+K_f}\Big]^2\Big). \tag{3.29}$$

Similarly, by substituting $r = 0$ in (3.12) the PDF can be obtained as

$$fa_\gamma(\gamma) = \frac{m^m}{\Gamma(m)}\frac{d_0}{2\sigma^2}\exp\Big(-\frac{\gamma}{2\sigma^2}\Big). \tag{3.30}$$

By substituting the value of the coefficient d_0 in (3.30), the expression of the asymptotic PDF of the FTR channel can be obtained as

$$fa_\gamma(\gamma) = \frac{m^m}{2\sigma^2}(m+K_f)^{-m} R_m\Big(\Big[\frac{K_f\Delta}{m+K_f}\Big]^2\Big)\exp\Big(-\frac{\gamma}{2\sigma^2}\Big), \tag{3.31}$$

where

$$R_m(x) = {}_2F_1\Big(\frac{m}{2}, \frac{m+1}{2}; 1; x\Big). \tag{3.32}$$

Asymptotic ASER of GFDM

The asymptotic expression of ASER for a GFDM system over the FTR fading channel can be calculated based on (3.16)

$$ASER_{asymp} = \int_0^\infty 2\left(\frac{p-1}{p}\right)\text{erfc}(\sqrt{\gamma_t}) f a_{\gamma_t}(\gamma_t) d\gamma_t - \int_0^\infty \left(\frac{p-1}{p}\right)\text{erfc}^2(\sqrt{\gamma_t}) f a_{\gamma_t}(\gamma_t) d\gamma_t, \tag{3.33}$$

Rewriting the above equation we get

$$ASER_{asymp} = S_{a1} - S_{a2}, \tag{3.34}$$

To derive the asymptotic expression of ASER, the integrals S_{a1} and S_{a2} must be evaluated. Substitute (3.31) into (3.33) gives

$$S_{a1} = 2\left(\frac{p-1}{p}\right)\int_0^\infty (1-erf(\sqrt{\gamma_t}))\left(\frac{m^m}{2\sigma^2}(m+K_f)^{-m} R_m\Big(\Big[\frac{K_f\Delta}{m+K_f}\Big]^2\Big)\exp\Big(-\frac{\gamma}{2\sigma^2}\Big)\right)d\gamma \tag{3.35}$$

Further Solving the expression of S_{a1} we obtain

$$S_{a1} = R_{a0}\int_0^\infty (1-erf(\sqrt{\gamma_t}))\exp\Big(-\frac{\gamma}{2\sigma^2}\Big)d\gamma \tag{3.36}$$

where

$$R_{a0} = 2\left(\frac{p-1}{p}\right)\left(\frac{m^m}{2\sigma^2}(m+K_f)^{-m} R_m\Big(\Big[\frac{K_f\Delta}{m+K_f}\Big]^2\Big)\Big)\right) \tag{3.37}$$

Now further solving the integral in (3.36) by using [**?**], Eq. (6.286), and Eq. (8.250), S_{a1} can be written as

$$S_{a1} = 2\Big(\frac{p-1}{p}\Big)\frac{m^m d_0}{\Gamma(m)}\frac{(1+K_f)}{\sqrt{\pi}\bar{\gamma}_t}, \tag{3.38}$$

Next, solving S_{a2} by substituting the value of $f a_{\gamma_t}(\gamma_t; r+1, 2\sigma^2)$ from (3.13) we get

$$S_{a2} = \left(\frac{p-1}{p}\right)\int_0^\infty \text{erfc}^2(\sqrt{\gamma_t})\left(\frac{m^m}{2\sigma^2}(m+K_f)^{-m} R_m\Big(\Big[\frac{K_f\Delta}{m+K_f}\Big]^2\Big)\exp\Big(-\frac{\gamma}{2\sigma^2}\Big)\right)d\gamma \tag{3.39}$$

Further Solving the expression of S_{a1} we obtain

$$S_{a2} = R_{a0}\int_0^\infty \text{erfc}^2(\sqrt{\gamma_t})\exp\Big(-\frac{\gamma}{2\sigma^2}\Big)d\gamma \tag{3.40}$$

The expression of S_{a2} can be solved using integration by parts, with $u = \text{erfc}^2(\sqrt{\gamma_t})$ and $dv = \exp\Big(-\frac{\gamma_t(1+K_f)}{\bar{\gamma}_t}\Big)$. After solving the integral in (3.40) , S_{a2} is written as

$$S_{a2} = \Big(\frac{p-1}{p}\Big)\frac{m^m d_0}{\Gamma(m)}\Big[1 - \frac{4}{\pi} \times {}_2F_1\Big(\frac{1}{2}, 1; \frac{3}{2}; \Big(\frac{-(1+K_f)}{\bar{\gamma}_t}\Big)\Big)\Big]. \tag{3.41}$$

By substituting (3.38) and (3.41) in (3.34), and substituting the values of d_0 and $R_m(x)$, the expression of asymptotic ASER is obtained as

$$\begin{aligned} ASER_{asymp} = \Big(\frac{p-1}{p}\Big)m^m(m+K_f)^{-m}{}_2F_1\Big(\frac{m}{2}, \frac{(m+1)}{2}; 1; \frac{K_f\Delta}{m+K_f}\Big) \\ \times \Big[\frac{2(1+K_f)}{\sqrt{\pi}\bar{\gamma}_t} - 1 + \frac{4}{\pi} \times {}_2F_1\Big(\frac{1}{2}, 1; \frac{3}{2}; \frac{-(1+K_f)}{\bar{\gamma}_t}\Big)\Big]. \end{aligned} \tag{3.42}$$

3.2 Results and discussion

The ASER expressions (3.28) and (3.42) derived in this chapter are numerically evaluated to analyze the performance of GFDM. Additionally, Monte Carlo simulations are provided for verification. From expressions (3.28) and (3.42), it is evident that ASER of the GFDM is influenced by fading channel parameters, the normalized instantaneous SNR, channel estimation errors, and the modulation order. Thus, the results are presented for various channels and system parameters.

Table 3.2: Simulation parameters.

Parameters	**Values**
Sub-carriers (K)	64
Sub-symbols (M)	9
Filter	Raised cosine (RC)
Mapping	16, 64 QAM
Cyclic Prefix	16
Roll-off factor (α)	0.9
Receiver	ZF
Channel estimation	Imperfect
Code rate (R_c)	1

The simulation results are provided for M = 9 subsymbols, K = 64 subcarriers and a CP of $K/4$. A raised cosine filter is used as a pulse-shaping filter with a roll-off factor of 0.9. Table 3.2 provides the values of system parameters utilized to evaluate the results presented in this section. The results are presented for the exact and asymptotic average SER of the GFDM systems. These results consider the effect of channel estimation error over the FTR fading

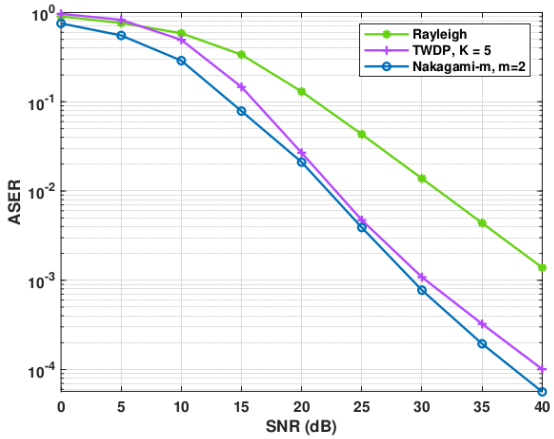

Figure 3.1: ASER for GFDM system for Rayleigh, TWDP and Nakagami-m channels as specific cases of FTR channel.

channel. Figure 3.1 illustrates the Rayleigh, TWDP (with $K = 5$), and Nakagami-m (with $m = 2$) fading channels as specific cases of FTR channel. ASER is evaluated for ${\varrho_A}^2 = 0$ using a 16-QAM modulation scheme.

The plot in the Figure 3.2 presents a plot depicting the relationship between ASER and SNR for a GFDM system. The plot showcases ASER's exact and asymptotic behaviours for a GFDM system with specific parameters: $\Delta = 0.9$, $K_f = 8$, and $m = 4$. Two different modulation schemes, 16-QAM and 64-QAM, are considered. Various values of the error parameter ${\varrho_A}^2 = 0, 0.01,$ and 0.03 are considered, and the results are plotted accordingly. For the 16-QAM scheme and a constant SNR of 25 dB, the ASER values are observed to be 8.54×10^{-3}, 1.66×10^{-2}, and 3.28×10^{-2} for ${\varrho_A}^2$ equal to 0, 0.01, and 0.03, respectively. Similarly, the plot reveals that for the 64-QAM scheme, the corresponding ASER values at SNR = 25 dB are 4.21×10^{-2}, 5.16×10^{-2}, and 7.05×10^{-2} for ${\varrho_A}^2$ equal to 0, 0.01, and 0.03, respectively. The example illustrates a noticeable degradation in performance of GFDM as channel estimation error increases. Furthermore, an increase in modulation order results in a decline in the system performance, as reflected in the ASER results.

Figure 3.3 presents the exact and asymptotic ASER versus E_s/N_o for an GFDM system with Δ = 0.1, K_f = 10, ${\varrho_A}^2 = 0.002$ and m = 3 & 5. The plots in Figure3.3 demonstrate how the ASER performance is affected by the channel parameter m variation in the presence of a channel estimation error of 0.002. The figure illustrates that an increase in the value of m from 3 (heavy fluctuations) to 5 (light fluctuations) mitigates the effects of channel fluctua-

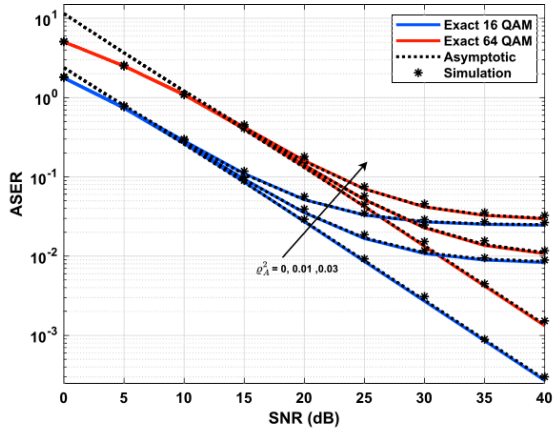

Figure 3.2: Exact and asymptotic ASER for GFDM system in FTR channel for $K_f = 8$, $\Delta = 0.9$, $m = 4$ and ${\varrho_A}^2 = 0, 0.01$ & 0.03

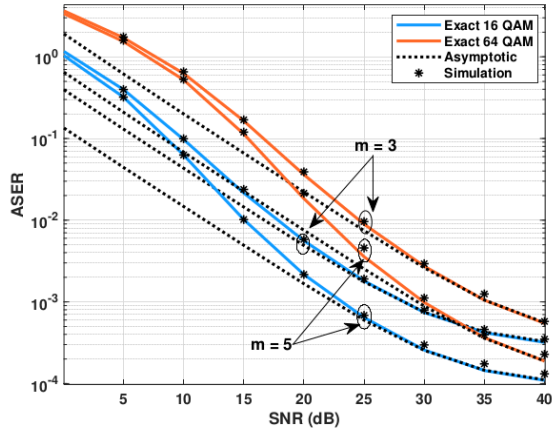

Figure 3.3: Exact and asymptotic ASER for GFDM system in FTR channel for $K_f = 10$, $\Delta = 0.1$, ${\varrho_A}^2 = 0.002$ and $m = 3$ & 5.

tions, resulting in improved ASER performance. When the parameter m decreases, the channel experiences significant fluctuations, leading to unfavourable fading conditions that further de-

teriorate the system's performance.

These curves also illustrate how variations in modulation order μ affect the system's performance. Let's consider the case of $m = 3$ and SNR = 20 dB, the ASER measured for 16-QAM is 5.60×10^{-3} and for 64-QAM modulation the ASER value is 3.60674×10^{-2}. The above data clearly shows that performance of GFDM degrades with increasing value of modulation order. As modulation order μ increases, more constellation points in the same space reduce the minimum Euclidean distance between them. A reduced minimum distance between symbols increases the likelihood of symbol confusion as the symbols are closer to each other. This heightened proximity also makes them more vulnerable to noise and interference, ultimately resulting in a higher ASER.

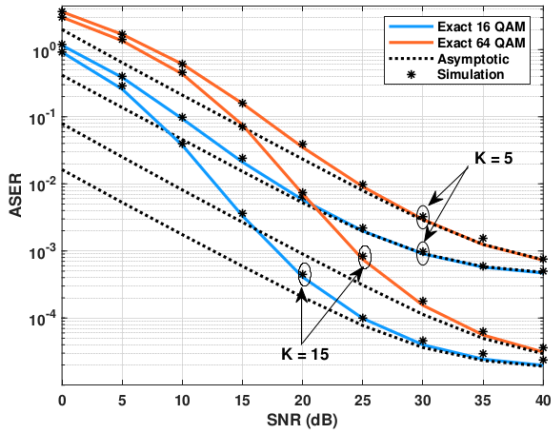

Figure 3.4: Exact and asymptotic ASER for GFDM system in FTR channel for m = 7, $\Delta = 0.1$, ${\varrho_A}^2 = 0.003$ and $K_f = 5$ & 15.

Figures 3.4 and 3.5 show the variations in ASER results for two parameters K_f and Δ, respectively, in the presence of channel estimation parameters. Figures 3.4 illustrate the impact of channel parameter variation, specifically the parameter K_f, on the ASER performance. These plots consider a channel estimation error of 0.003, m = 7, $\Delta = 0.1$ and $K_f = 5$ & 15. The curves provide clear evidence of the improvement in ASER for larger values of K_f. A higher value of K_f indicates that the total power of the dominant components (line of sight component) is more significant than the power of the scattered waves (fading component). This, in turn, will mitigate the fading effect of the channel. For instance, when using 16 QAM modulation with a SNR of 15 dB, the ASER decreases from 2.10746×10^{-2} to 3.32772×10^{-3} as the channel parameter K_f increases from 5 to 15. Similarly, for 64 QAM modulation considering SNR =

15 dB, the ASER decreases from 1.5724×10^{-1} to 7.53885×10^{-2} as K_f increases from 5 to 15.

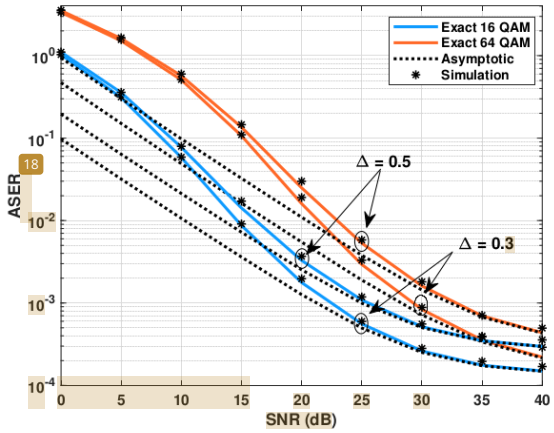

Figure 3.5: Exact and asymptotic ASER for GFDM system in FTR channel for $m = 7$, $K_f = 10$, ${\varrho_A}^2 = 0.004$ and $\Delta = 0.3$ & 0.5.

Conversely, in Figure 3.5, the ASER experiences a slight deterioration as Δ increases from 0.3 to 0.5. This occurs because an increase in Δ leads to a more significant phase difference between the two primary waves, ultimately intensifying the severity of channel fading. Figure 3.5 presents ASER of GFDM for channel parameters $m = 7$, $K_f = 10$, $\Delta = 0.3$ & 0.5 and the channel estimation error of 0.004. As the figure depicts for a 16-QAM GFDM system at 30 dB SNR, the ASER increases from 2.61489×10^{-4} to 5.1567×10^{-4} as the value of Δ increases from 0.3 to 0.5. The performance of a 64-QAM GFDM system deteriorates as shown in the figure, the ASER rises from 8.33105×10^{-4} to 1.60762×10^{-3} as the value of Δ increases from 0.3 to 0.5 while maintaining SNR at 30 dB.

3.3 Summary

This chapter explores performance of the GFDM under FTR fading scenario for μ QAM modulation schemes. Both exact and asymptotic ASER expressions are derived, with the analytical results numerically evaluated and validated through Monte Carlo simulations.

Chapter 4

Synchronization technique for GFDM based 5G communication System

In GFDM, the non-orthogonality of subcarriers and the block-based structure make synchronization more challenging compared to traditional schemes like OFDM. Accurate synchronization ensures proper alignment of time and frequency domains, enabling reliable data transmission and reception. Timing offsets, carrier frequency offsets (CFO), and phase noise can lead to inter-symbol interference (ISI) and inter-carrier interference (ICI), significantly deteriorating system performance. A critical factor in enhancing the performance of GFDM is achieving precise synchronization.

To that end, a new timing synchronization algorithm that utilizes cross-correlation and the sliding window algorithm is presented in this article. The algorithm uses a training symbol based on a chirp sequence. The simulation results of proposed estimator and conventional CP based approach are analyzed for indoor office scenarios and urban macro cells scenarios for OFDM and GFDM. Performance of proposed method is analyzed for GFDM based on three parameters: mean timing offset, mean square error (MSE), and probability of timing failure.

Section 4.1 discusses the symbol timing offset analysis for the GFDM system, followed by the various timing offset estimation methods in Section 4.2. The GFDM system model and the training symbol used for the synchronization of the GFDM system are detailed in Section 4.3. Further, Section 4.4 presents proposed timing estimation technique for the GFDM system. Section 4.5 presents performance evaluation of proposed estimator, while Section 4.6 wraps up the chapter with a summary.

4.1 Symbol Timing Offset Analysis for GFDM

Symbol Timing Offset (STO) refers to the misalignment between the transmitter's and receiver's symbol boundaries, which can lead to performance degradation in communication systems. This offset occurs when the receiver's timing reference does not accurately match

the transmitted signal's symbol boundaries, leading to degraded system performance. Incorrect symbol timing can cause overlap between adjacent symbols, introducing ISI and degrading error performance. Misaligned timing affects the sampling point, leading to decreased signal detection accuracy. The received signal with a timing offset, t, can be formulated as:

$$r(h) = s(h - t) + n(h) \tag{4.1}$$

In the above equation $r(h)$ and $s(h)$ represents the transmitted and received signals, respectively. $n(h)$ is the additive noise and t is the timing offset.

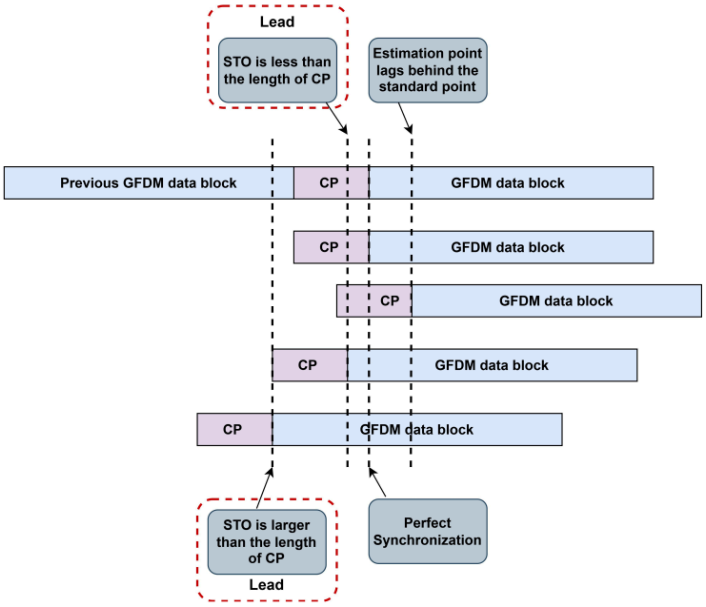

Figure 4.1: Symbol timing offset analysis.

Timing errors can arise due to differences in clock frequencies between the transmitter clock and receiver clock, a phenomenon known as clock mismatch. Additionally, multipath propagation and delay spread in fading channels can distort timing alignment, further complicating the synchronization process. Background noise and interference also play a significant role, as they can disrupt the accurate detection of symbol boundaries, leading to performance degradation. Misaligned timing leads to ISI, where adjacent symbols overlap and degrade the signal quality. Incorrect sampling points further reduce the accuracy of signal demodulation, exacerbating performance issues. This results in increased error rates, such as SER. Moreover, STO

can intensify the impact of other impairments, including CFO and phase noise, compounding the overall degradation in system performance.

In GFDM, the block-based structure and the use of non-orthogonal subcarriers make the system particularly sensitive to timing errors, making STO analysis critical for maintaining reliable operation. Due to the block structure of GFDM, STO disrupts the alignment of the GFDM block, leading to cumulative errors across subcarriers and subsymbols. Circularly shifted pulse shaping in GFDM helps mitigate the impact of STO by localizing energy within subcarriers. Analyzing STO is crucial for assessing and enhancing GFDM system performance, especially in environments with high mobility or multipath propagation. Robust synchronization techniques must address STO to ensure reliable communication in next-generation networks like $5G$.

In Figure 4.1, the first case demonstrates that the estimation point perfectly aligns with the ideal timing reference, indicating no timing offset. As a result, the receiver accurately identifies the start of each GFDM data block. In the second case, the receiver's timing estimation falls behind the ideal timing reference, causing current GFDM data block to extend into the subsequent block. In the third case, the receiver's timing estimation point occurs earlier than the standard timing point but remains within the CP range. In the final case, the receiver's timing estimation point surpasses the standard timing point by an amount greater than the CP length.

4.2 Timing Offset Estimation Methods

Timing offset estimation is a critical process in communication systems to ensure accurate synchronization between the transmitter and receiver. In multicarrier systems like GFDM and OFDM, precise timing alignment is essential to prevent ISI and maintain signal integrity. Timing offsets arise from various factors, including clock mismatches, multipath propagation, and dynamic channel conditions, making their estimation and correction a significant challenge. To address this, various timing offset estimation methods have been developed, each tailored to specific system requirements and operating scenarios. Each method offers a unique balance between complexity, accuracy, and overhead, ensuring adaptability to diverse environments, from static IoT networks to high-mobility 5G scenarios. This section provides an overview of the different timing offset estimation techniques and their applicability in modern communication systems.

4.2.1 CP Based Methods

The CP-based method utilizes the CP in multicarrier systems such as GFDM and OFDM for synchronization. The CP is a copy of the last portion of the data symbol appended at beginning of each transmitted symbol. This redundancy creates a repetitive pattern. The receiver compares the CP with the corresponding part of the data symbol. A high correlation indicates the

presence of the CP and marks the potential start of a new data block. By utilizing the existing CP, this method eliminates the need for additional sequences like preambles.

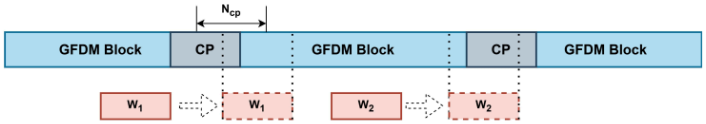

Figure 4.2: CP-based synchronization model.

Figure 4.2 illustrates the synchronization model based on the CP. The CP length is represented by N_{cp}. Two sliding windows, W_1 and W_2, each with a length of N_{cp}, shift sequentially from the beginning to the end, moving one point at a time. The distance between W_1 and W_2 corresponds to length of GFDM data block. Slide both windows point by point over the received signal. For each position, compute the correlation between the data in W_1 and W_2. A high correlation value indicates that the windows are aligned with the CP and its corresponding data portion, suggesting the start of a new symbol. STO detection is performed by detecting peak of cross-correlation coefficient.

In the CP based method, the timing metric has a large plateau rather than a distinct peak due to the presence of similar values near the offset value, leading to a higher error value in the timing offset estimation. To address these limitations, the next section introduces a pilot-based synchronization approach.

4.2.2 Pilot-Based Synchronization

Pilot-based synchronization is commonly employed method in communication systems, including GFDM, to achieve accurate timing and frequency synchronization. This method employs known pilot symbols (PS) embedded within the transmitted data frame to aid the receiver in synchronization tasks. Pilot symbols are predefined and known to both the transmitter and receiver. Pilots can be inserted at regular intervals within the data frame or as dedicated pilot blocks, depending on the system design.

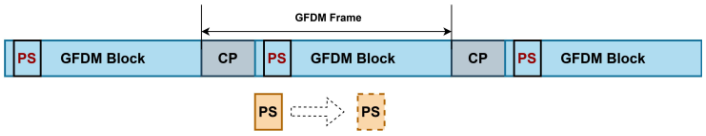

Figure 4.3: Pilot-based Synchronization.

The pilot-based synchronization model is shown in Figure 4.3. Pilot symbols are predetermined sequences that are recognized by both the transmitter and receiver. These symbols are strategically placed within the transmitted data frame to facilitate synchronization by providing

reference points for timing and frequency estimation. The receiver scans the incoming signal for the known pilot symbols. A correlation process is carried out between the received signal and the predefined pilot sequence.The correlation peak signifies the presence of pilot symbols and aids in estimating the timing offset.

This method provides precise timing and frequency synchronization due to the known nature of pilot symbols. Pilots can be used to continuously monitor and adjust synchronization, reducing the impact of drift. Pilots facilitate not only synchronization but also channel estimation and equalization. However, the need for pilot symbols reduces the available bandwidth for data transmission. Also, in multipath environments, interference from other signals can corrupt pilot symbols, leading to inaccurate synchronization. To address these limitations, the next section introduces a preamble-based synchronization approach.

4.2.3 Preamble-Based Methods

Preamble-based techniques are commonly utilized for timing offset estimation in communication systems. These methods rely on sending a preamble sequence, designed with high correlation properties, which is transmitted before the data frame. The receiver determines the timing offset by computing the cross-correlation of received signal and preamble. Based on the correlation peak, the timing offset is estimated, enabling the receiver to accurately align the symbol boundaries.

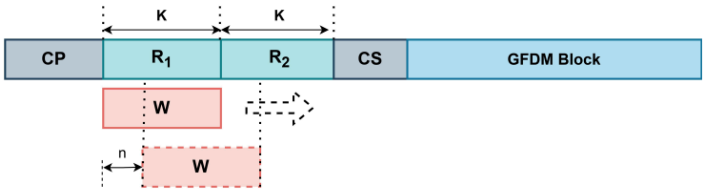

Figure 4.4: PN-based Synchronization.

The preamble consists of a predefined, known sequence that is easily detectable and exhibits strong correlation properties. It is designed to minimize cross-correlation with other parts of the signal and maximize auto-correlation at zero lag, thereby enhancing detection accuracy. Various types of pseudo-noise (PN) sequences are used, such as shift register sequences, Gold sequences, GMW sequences, and chirp signals. Among these signals chirp sequence has good auto-correlation and spectral characteristics

The preamble sequence in Figure 4.4 consists of two identical PN sequences, R_1 and R_2, each with a length of K. A sliding window W, also of length K, moves point by point across the sequence. At each position, cross-correlation coefficient is calculated between the segment of W and local PN sequence. The peak value of this cross-correlation helps in estimating the

starting sample of the PN sequence. After estimating the PN sequence, the data symbol can be easily localized.

4.3 System Description

4.3.1 GFDM Signal Generation

The GFDM system considered in the present analysis is shown in Figure 2.1. The transmitter in this system employs a mapper that converts the input binary data into complex data symbol $d_{k,m}$ using either μ-QAM or μ-PSK modulation technique. This serial complex data symbol is then given to the GFDM modulator, which processes the N-data symbol in parallel by decomposing it into K number of sub-carriers and M number of sub-symbols (i.e. $N = KM$). The output of the GFDM modulator is written as

$$x(n) = \sum_{k=0}^{K-1} \sum_{m=0}^{M-1} d_{k,m} \cdot g_{k,m}(n), \quad n = 0, ..., N-1 \tag{4.2}$$

Where $\mathbf{d}_{k,m}$ is symbol corresponding to k^{th} sub carrier and m^{th} sub-symbol, μ is modulation order, each $\mathbf{g}_{k,m}[n]$ represents time and frequency-shifted variant of $\mathbf{g}[n]$, that can be written as

$$\mathbf{g}_{k,m}(n) = g\Big[(n - mk) \mod N\Big] \cdot \exp\left[-j\frac{k}{K}2\pi n\right] \tag{4.3}$$

In this context, modulo operation and complex exponential signify circular and frequency shifting, respectively. After this, a CP of N_{cp} samples is appended to $\mathbf{x}(n)$ to produce $\mathbf{x}_c(n)$.

4.3.2 Training Signal Generation

For the proposed timing estimation technique, a novel training symbol is designed using a chirp sequence to achieve high accuracy in locating peak value of timing metric at receiver. The reason for using the chirp sequence is its good auto-correlation and spectral characteristics [**?**]. The chirp sequence exhibits zero correlation with its cyclically shifted version, making it an ideal choice for time synchronization.

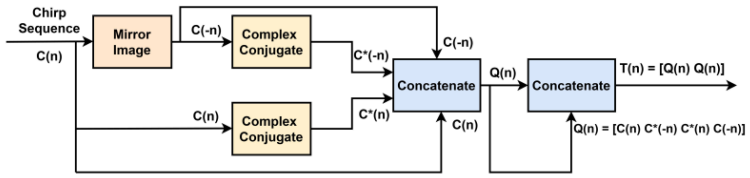

Figure 4.5: Proposed Training Signal Generator Block

The steps for the generation of the proposed training signal are shown in Figure 4.5. This training signal generation block takes a discrete chirp sequence $C(n)$ as an input, which can be defined as

$$C(n) = a_o \exp\left[j2\pi\left(\beta_o \frac{n^2}{N}\right)\right], \quad n = 0, 1, ...(K/8) \tag{4.4}$$

where K is the length of the training symbol, a_o and β_o represent the magnitude and modulation rate of the chirp signal, respectively. This chirp sequence $C(n)$ of length $K/8$ is then given to the mirror image block to generate the mirror image $C(-n)$. After this, complex conjugate of both $C(n)$ and $C(-n)$ is calculated, resulting in $C^*(n)$ and $C^*(-n)$, respectively. These four values are then concatenated to create one-half of the training symbol $Q(n)$, which is represented as

$$Q(n) = [C(n) \quad C^*(-n) \quad C^*(n) \quad C(-n)] \tag{4.5}$$

Now, this sequence $Q(n)$ is given as input to the identical image block, which generates the proposed training symbol $T(n)$ by concatenating $Q(n)$ by itself. The structure of the proposed training symbol can be given by

$$T(n) = [Q(n) \quad Q(n)] \tag{4.6}$$

Figure 4.6 illustrates the phase and amplitude of the training symbol.

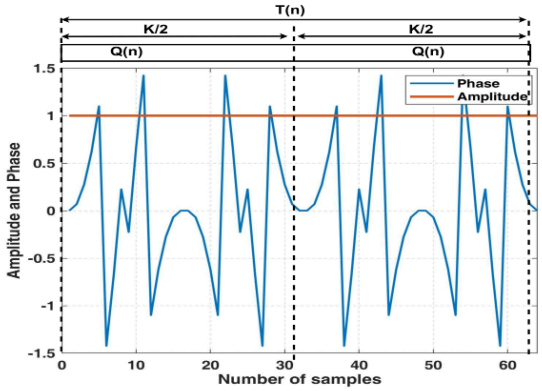

Figure 4.6: The phase and amplitude of training symbols.

4.3.3 Received Signal description

Taking into account the impact of the multipath fading, received signal $\mathbf{y}_c(n)$ is expressed as

$$y_c(n) = \sum_{l=0}^{L-1} h(l) \cdot \mathbf{x}_c(n-l), \quad n = 0, ..., KM-1 \tag{4.7}$$

here $h(l)$ denotes impulse response of channel for l^{th} path, while L presents the total number of multipath. The timing offsets on the receiver side are represented as a delay in the received signal. After considering the timing offset and noise, the (4.7) can be rewritten as

$$\mathbf{r}_c(n) = \mathbf{y}_c(n-p) + \mathbf{w}(n) \tag{4.8}$$

where p represents the unknown arrival time of symbol, and $\mathbf{w}(n)$ represents the complex AWGN with mean equal to 0 and $\sigma^2{}_w$ variance. Main objective of any timing synchronization technique is to determine value of this delay p. The proposed timing estimation technique is presented in next section.

4.4 Proposed Timing Estimation Technique

The proposed timing estimation technique utilizes cross-correlation and the sliding window algorithm. At the receiver, the input received data is given to the timing synchronization block, which generates a timing metric $F(b)$ by correlating the received data with the locally generated training symbol. The peak value of this calculated timing metric helps in estimating starting sample of the training symbol. After estimating this training symbol, the data symbol can be easily localized.

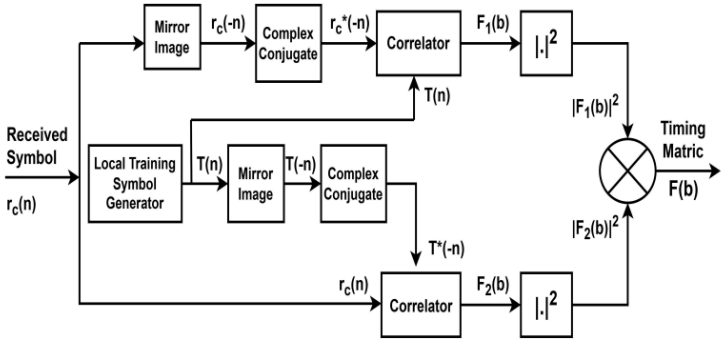

Figure 4.7: Timing Synchronization Block

The proposed timing synchronization block is shown in Figure 4.7, which consists of two parallel sub-blocks. The algorithm for generating the timing metric is explained below

- The upper sub-block performs cross-correlation of locally generated training symbol $T(n)$ with K samples of flipped conjugate received signal $r_c^*(-n)$. The output of this correlator can be represented as:

$$F_1(b) = \sum_{n=0}^{K-1} r_c^*(b - n + K) \cdot T(n) \tag{4.9}$$

  here b is the timing index which represents b^{th} sample of GFDM frame over a window of length K.

- At the same time, another sub-block is operated in parallel to perform the correlation between the received symbol $r_c(n)$ and the flipped conjugate of the local training sequence $T_c^*(-n)$. The output of this correlator can be represented as

$$F_2(b) = \sum_{n=0}^{K-1} r_c(b + n) \cdot T^*(K - n) \tag{4.10}$$

- After correlation, the square operation on the absolute value of both correlators is performed.

- The output of both the sub-blocks are then multiplied to generate the final timing metric $F(b)$, which is presented by

$$F(b) = |F_1(b)|^2 \cdot |F_2(b)|^2 \tag{4.11}$$

- This procedure is repeated for every K samples of the received signal.

- By detecting peak of resulting timing metric $F(b)$, initial point (b_{max}) of the received training symbol can be estimated as

$$b_{max} = \arg\left(\max_b(F(b))\right) \tag{4.12}$$

To demonstrate the proposed algorithm, an example of a GFDM system with a frame length of 432 samples is considered here, as illustrated in Figure 4.8. The frame begins with a training symbol of 88 samples (including 16 samples of CP and 8 samples of CS), followed by a GFDM symbol of length 344 samples (including 16 samples of CP and 8 samples of CS). The GFDM frame parameters are shown in Table 4.2.

The timing metric generated using the proposed algorithm is shown in Figure 4.9. No noise and channel conditions have been considered to generate this timing metric. For comparison,

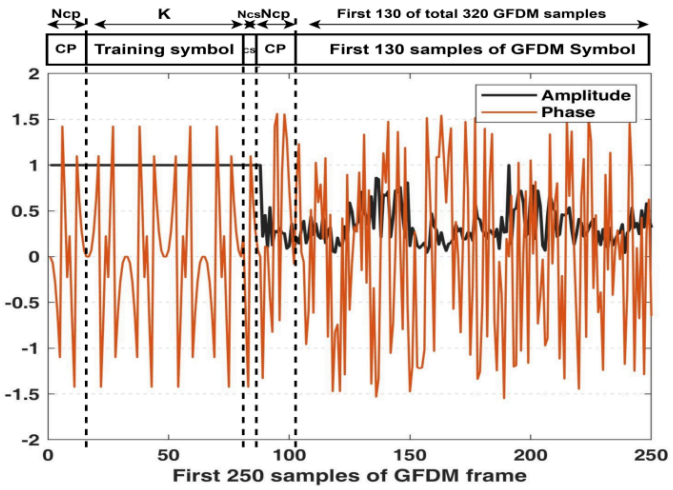

Figure 4.8: An example of GFDM Frame with N = 320, K = 64, M = 5, Ncp = 16 and Ncs = 8

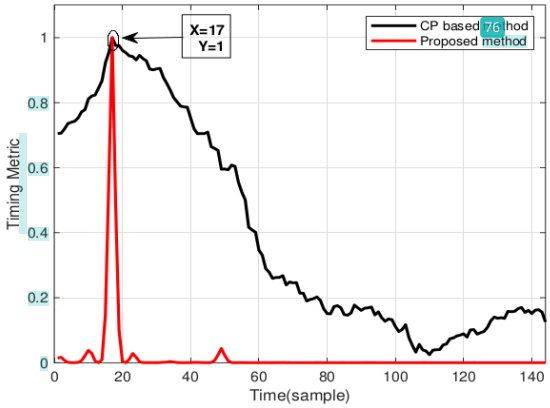

Figure 4.9: Timing metric for proposed and CP based estimator.

the CP based estimator as given in [**?**] is also considered here. It is depicted from Figure 4.9 that although the maximum value of timing metric with both the schemes is coinciding at the same sample $(N_{cp}+1)^{th}$ (17^{th}), however, the peak generated with the proposed algorithm is sharp as compared to the CP based method.

4.5 Performance analysis

This section presents the performance analysis of proposed estimator. The mean and the MSE of timing offset and probability of the timing failure are considered performance evaluation parameters. The proposed estimator's performance is compared to the CP-based STO estimation technique.

Table 4.1: Simulation parameters for the OFDM.

Parameters	**Values**
Filter	Rectangular Filter
Modulation scheme	16 QAM
Number of subcarriers	64
Length of CP (Ncp)	16
Length of CS (Ncs)	8

For the proposed training symbol and CP based method, the error of STO estimation is evaluated for 10^5 realizations at each SNR value. The results for performance evaluation are given for both the OFDM and GFDM systems. The parameters used in the simulation for OFDM and GFDM systems are given in Table 4.1 and Table 4.2, respectively.

Table 4.2: Simulation parameters for the GFDM.

Parameters	**Values**
Pulse Shaping Filter	Raised Cosine (RC)
Roll off factor	0.2
Modulation scheme	16 QAM
Number of subsymbols (M)	5
Number of subcarriers (K)	64
Length of CP (Ncp)	16
Length of CS (Ncs)	8

The channel considered for the performance analysis is the TDL-B tapped delay line model of the 3GPP $5G$ channel model and is evaluated under two different scenarios: indoor office and UMa cells [**?**]. The TDL-B channel model is a non-line-of-sight (NLOS) model and is scaled in the delay to achieve the required RMS delay spread. The RMS delay spread for the indoor office scenario is 39 ns, while for UMa, it is 363 ns [**?**].

4.5.1 Mean and Mean Square Error

Figures 4.10 and 4.11 illustrate the mean and MSE of the timing offset, respectively, in indoor office scenarios for both OFDM and GFDM systems. It is evident from Figure 4.10 that the

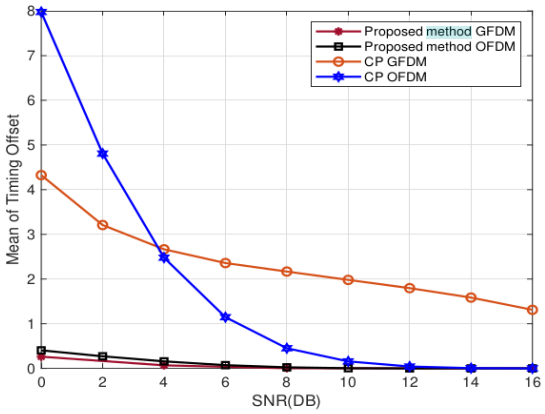

Figure 4.10: In indoor office scenario, the means versus SNRs of both estimators for OFDM and GFDM.

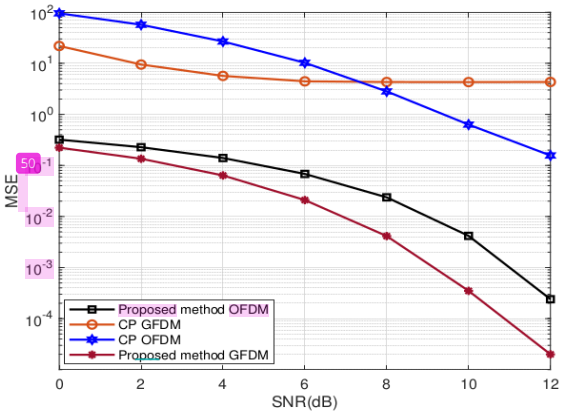

Figure 4.11: In indoor office scenario, the MSE versus SNRs of both estimators for OFDM and GFDM.

mean error value of timing offset estimation is much lower for the proposed method than the CP based method for both GFDM and OFDM. The reason behind the low mean error value in the proposed chirp signal-based method for timing offset estimation is the presence of a sharp peak in its timing metric. On the other hand, in the CP based method, the timing metric has a large plateau instead of a distinct peak due to presence of similar values near the offset value, leading to a higher mean error value in the timing offset estimation. As shown in Figure 4.11, the proposed method achieves better performance than the CP-based approach in terms of the MSE of the timing offset for both GFDM and OFDM systems. Similarly, in the case of

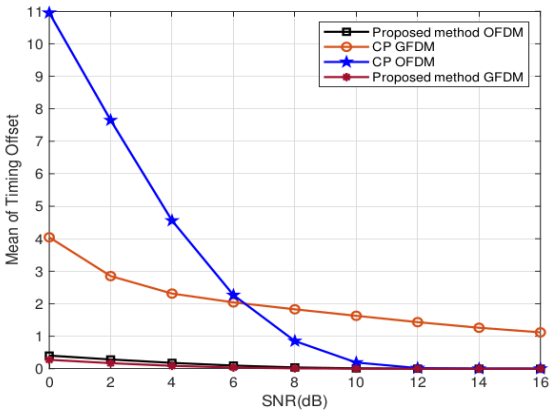

Figure 4.12: In urban macrocell scenarios, the means versus SNRs of both estimators for OFDM and GFDM.

UMa cells, the graph illustrates the relationship between the mean timing offset error and SNR for both OFDM and GFDM systems using the proposed and CP-based methods is illustrated in Figure 4.12. The plots indicate that the proposed method achieves superior performance compared to the CP-based approach in both systems.

Figure 4.13 illustrates MSE of timing offset estimation for both schemes in OFDM and GFDM systems within the UMa cells scenario. In terms of MSE, the performance of GFDM for CP based method is better than OFDM for lower values of SNR. Compared to all the other curves, the proposed estimator provides a superior MSE.

4.5.2 Probability of Timing Failure

The timing metric $F(b)$ is utilized in the received signal to identify the starting point of the training sequence, therefore, the peak in the timing metric corresponds to the start of the training sequence. Ideally, the expected peak of the timing metric is anticipated to appear at the

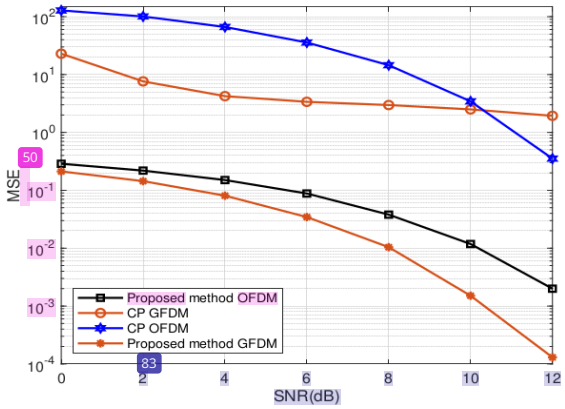

Figure 4.13: In urban macrocell scenarios, the MSE versus SNRs of both estimators for OFDM and GFDM.

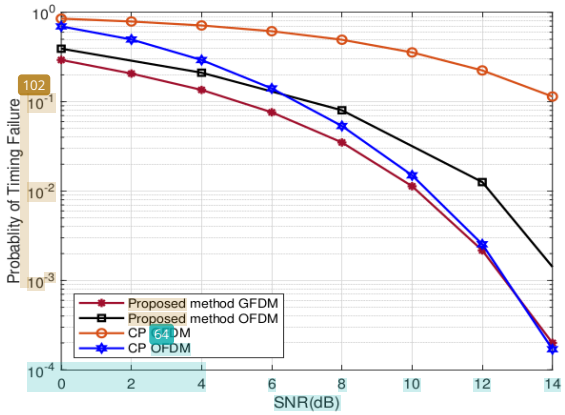

Figure 4.14: Probability of timing failure versus SNR of both estimators in indoor office scenario for OFDM and GFDM.

$(Ncp + 1)^{th}$ sample. However, in communication systems, the actual location of the peak is uncertain in practice. It may deviate from the expected location due to channel fading or noise. These disturbances make it challenging to locate the peak, which makes timing synchronization unfeasible.

To make this procedure feasible, it is assumed that the peaks are deterministic and occur at the $(Ncp+1)^{th}$ sample, which, in our case, is at the 17^th position. A predefined threshold value $\gamma \in (0, 1)$ is considered, and the timing metric is compared with the threshold. The probability of timing failure in a single comparison is the probability that the event $F(Ncp + 1) < \gamma$ occurs. It means that peak of timing metric is lower than predefined threshold value, and it will not detect the correct location of the training sequence's beginning point, resulting in the event of synchronization failure. If $F(Ncp + 1) > \gamma$, meaning peak of timing metric is above predefined threshold value, then the correct location of the training symbol will be detected.

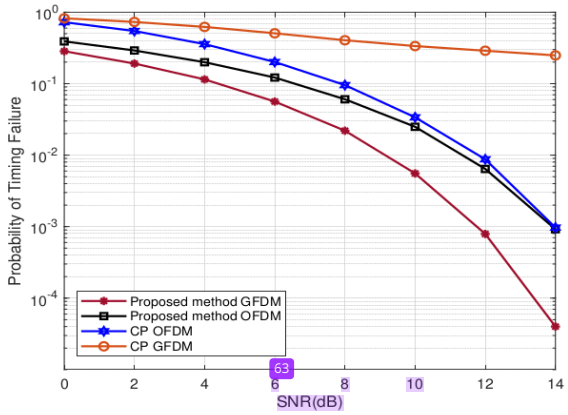

Figure 4.15: Probability of timing failure versus SNR of both estimators in urban macro cells scenario for OFDM and GFDM.

Figure 4.14 presents a comparison of the probability of failure for proposed method and CP-based approach for OFDM and GFDM in an indoor office scenario. The graph indicates that the performance of the CP-based estimator for GFDM is inferior. Moreover, the CP-based OFDM system performs inferior to the proposed OFDM system at lower SNR values. At higher SNR values, it performs comparably well to the proposed GFDM system. The proposed GFDM system outperforms all other curves.

Figure 4.15 illustrates the probability of timing failure for OFDM and GFDM systems in the UMa cells scenario using the two discussed techniques. It is apparent that for lower SNR values, the proposed method outperforms the CP-based synchronization approach for the OFDM system. Furthermore, the proposed estimator's performance is considerably better than the CP-based approach for both OFDM and GFDM systems.

4.6 Summary

This chapter proposes an improved approach for estimating the timing offset of signals in GFDM systems, utilizing a chirp signal as a training symbol. The chapter evaluates the performance of the two synchronization techniques in both indoor office and urban macro (UMa) cell scenarios, with simulation results provided for both OFDM and GFDM communication systems. The proposed methodology can be extended beyond OFDM and GFDM systems and adapted to other waveforms and systems such as NOMA, FBMC, UFMC, and OTFS. Furthermore, the algorithm's effectiveness has been assessed on two channels, indicating its potential to be evaluated on various channels and eventually utilized in 6G wireless communication systems.

Chapter 5

Performance Improvement of GFDM based 5G and beyond communication System

Future next-generation wireless communication systems will face a wide range of requirements, including data rates exceeding those of fifth-generation networks, ultra-low power consumption for battery-powered communication sensors, and minimal response times critical for control applications. A key characteristic of the GFDM system is its use of flexible pulse-shaping filters in the time domain, allowing it to meet the diverse demands of modern communication systems. Choosing an appropriate filter is crucial for the OOB radiation and SER performance of the GFDM system. Therefore, designing a well-localized pulse-shaping filter significantly impacts OOB emissions and enhances SER performance in the GFDM system.

.

This chapter presents the design of a pulse-shaping filter for the GFDM system, utilizing discrete Gabor representation, biorthogonality conditions, and WD. An analytical formulation for the analysis window is obtained based on the biorthogonality condition. Additionally, the GFDM system's performance is evaluated in terms of OOB radiation and SER. The results are provided for the QAM scheme across AWGN, Rayleigh, Nakagami-m, TWDP, and Nakagami-q fading channels. A comprehensive analysis reveals that OOB radiation and SER performance are highly influenced by the selection of the pulse-shaping filter.

Section 5.1 discusses the system model for the GFDM system, followed by a detailed description and mathematical analysis of the proposed pulse shaping filter in Section 5.2. The performance analysis of the proposed filter for the various fading channels is presented in Section 5.3, and Section 5.4 concludes the chapter with a summary.

5.1 System model

The baseband GFDM system model used in this analysis is illustrated in Figure 5.1. In this system, N complex data symbols are initially converted into parallel form using a serial-to-parallel converter and then decompose into K sub-carriers, each containing M sub-symbols ($N = KM$), by the GFDM modulator. The GFDM modulator produces an output that can be represented as [?]

$$x[n] = \sum_{k=0}^{K-1} \sum_{m=0}^{M-1} d_{k,m} g_{k,m}[n], \quad \text{for } n = 0, 1, ..., N-1 \tag{5.1}$$

here $\mathbf{d}_{k,m}$ presents μ-QAM modulated complex data symbol transmitted on k^{th} sub-carrier in m^{th} sub-symbol of every GFDM block, and the term $\mathbf{g}_{k,m}[n]$ refers to frequency and time-shifted version of $g[n]$ which is pulse shaping filter, is represented as [?]

$$\mathbf{g}_{k,m}[n] = g[(n - mk) \text{mod} N] \cdot \exp[-j2\pi kn/K] \tag{5.2}$$

The signal $x[n]$ after modulation can be represented as vector $\mathbf{x} = [x(0), x(1), \ldots, x(n-1)]^T$. Thus (5.1) can be reformulated in matrix notation, as elaborated in [?] as

$$\mathbf{x} = \mathbf{Ad} \tag{5.3}$$

here the matrix $\mathbf{A}$ represents GFDM transmitter matrix of dimensions $N \times N$, that can be represented in terms of filter coefficients $g[n]$ as follows [?]

$$\mathbf{A} = [\mathbf{g}_{0,0}, \cdots \mathbf{g}_{K-1,0} \quad \mathbf{g}_{0,1}, \cdots \mathbf{g}_{K-1,1} \quad \mathbf{g}_{0,M-1}, \cdots \mathbf{g}_{K-1,M-1}] \tag{5.4}$$

where vector $\mathbf{g}_{k,m}$ represents $(\mathbf{g}_{k,m}[n])^T$. A CP is appended to transmission signal to get the final symbol vector $\mathbf{x}_{cp}$.

At the receiver side, assuming perfect synchronization and subsequent removal of the cyclic prefix, the received signal is represented as

$$\mathbf{y} = \mathbf{Hx} + \mathbf{w} \tag{5.5}$$

In this context, $\mathbf{H}$ represents the channel matrix, which takes the form of an $N \times N$ convolution matrix. The vector $\mathbf{w}$ corresponds to the noise, where each element signifies an i.i.d complex Gaussian random variable (mean = 0, variance = σ^2). Considering perfect channel estimation, received signal with channel equalization can be written as [?]

$$\begin{aligned} \mathbf{z} &= \mathbf{H}^{-1}\mathbf{y} = \mathbf{H}^{-1}\mathbf{Hx} + \mathbf{H}^{-1}\mathbf{w} \\ &= \mathbf{x} + \mathbf{H}^{-1}\mathbf{w} = \mathbf{Ad} + \mathbf{H}^{-1}\mathbf{w} \end{aligned} \tag{5.6}$$

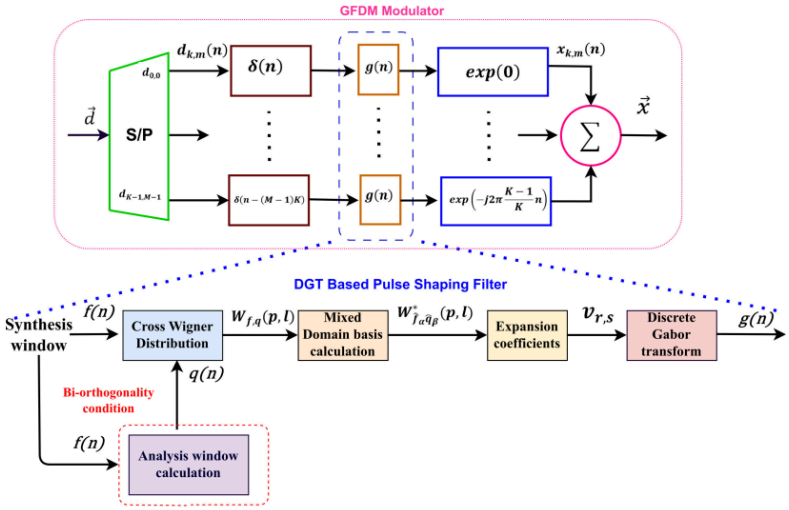

Figure 5.1: GFDM modulator with proposed pulse shaping filter

The signal's linear demodulation is represented as

$$\mathbf{z} = \mathbf{BAd} + \mathbf{BH}^{-1}\mathbf{w} \tag{5.7}$$

where **B** is the receiver matrix. Here, a ZF ($\mathbf{B} = \mathbf{A}^{-1}$) receiver is used, which eliminates self-interference at receiver but enhances noise.

5.2 Proposed pulse shaping filter

GFDM offers flexibility in selecting pulse shaping filters $g[n]$, significantly influencing the system's spectral properties and SER performance. So, in this section, a filter design is proposed utilizing the Wigner distribution, Wexler-Raz equation, and discrete Gabor representation. The suitability of the Wigner distribution for signal processing arises from its ability to address nonstationarities and time-varying characteristics in signals effectively. The objective is to determine a time sequence, $g[n]$, using the expansion coefficient. This expansion coefficient is determined in a manner that ensures the Wigner distribution $\mathbf{W}_{f,q}(p,l)$ closely approximates $Y(p,l)$ in the least squares sense, where $Y(p,l)$ is the desired periodic function specified in the

Wigner domain. The error function (ϵ) that needs to be minimized is as follows [**?**]

$$\begin{aligned}\epsilon &\triangleq \langle Y - \mathbf{W}_{f,q}, Y - \mathbf{W}_{f,q}\rangle \\ &= 4R_1 \sum_{p=0}^{R_1-1}\sum_{l=0}^{R_1-1}[\mathbf{Y}(p,l) - \mathbf{W}_{f,q}(p,l)]\cdot \\ &\qquad [\mathbf{Y}^*(p,l) - \mathbf{W}^*_{f,q}(p,l)] \end{aligned} \tag{5.8}$$

From this point onwards, $Y(n,m)$ is assumed to be a real-valued function since minimizing Y and Y_R results in the same time sequence. The desired periodic function, in our case, is the Gaussian window, as it possesses several outstanding features. Using a Gaussian window produces a time-frequency basis characterized by a decay that follows an asymptotic algebraic pattern of $(1/\omega, 1/t)$. The more general case of oversampling is considered here, as it leads to mathematical simplicity and helps in clear interpretation. When dealing with noisy data, it is crucial to have a certain level of oversampling, similar to the well-known concept of Fourier-Nyquist sampling. Let R, $\overline{R}$, S, and $\overline{S}$ be positive integers constrained by

$$R_1 = R.\overline{S} = \overline{R}.S \tag{5.9}$$

For oversampling, $R \leq RS$ is considered. Let $g[n]$ represent a periodic time sequence which represents pulse shaping filter of GFDM. The discrete Gabor expansion is given as

$$g[n] = \sum_{r=0}^{R-1}\sum_{s=0}^{S-1} z_{r,s}\hat{f}_{r,s}[n] \tag{5.10}$$

The R denotes the time resolution, while the symbol S represents the frequency resolution. The Gabor coefficient $z_{r,s}$ can be calculated as

$$z_{r,s} = \sum_{n=0}^{R_1-1} g[n]\hat{q}^*_{r,s}[n] \tag{5.11}$$

where $\hat{f}_{r,s}[n] \triangleq f(n - \overline{R}s)W^{rn}$, $W \triangleq exp(i2\pi/S)$, $\hat{q}_{r,s}[n] \triangleq \tilde{q}(n - \overline{R}s)W^{rn}$, and $\vec{f}$ represents the "synthesis" window subjected to the energy normalization

$$\sum_{n=0}^{R_1-1} |f[n]|^2 \tag{5.12}$$

The sequence $\vec{q}$ represents the "analysis" window which satisfies the bi-orthogonality condition. Consequently, $f[n]$ and $q[n]$ can be interchanged in (5.10), leading to an alternative

representation of $g[n]$ as

$$g[n] = \sum_{r=0}^{R-1} \sum_{s=0}^{S-1} v_{r,s} \hat{q}_{r,s}[n] \tag{5.13}$$

So the Gabor coefficient $z_{r,s}$ can now be replaced with the new Gabor coefficient $v_{r,s}$ which is now defined as

$$v_{r,s} = \sum_{n=0}^{R_1-1} g[n] \hat{f}^*_{r,s}[n] \tag{5.14}$$

Solving the discrete bi-orthogonality condition is crucial for the computation of the analysis window $q(n)$ in terms of synthesis window. The bi-orthogonality condition in the case of oversampling can be expressed as [**?**]

$$\sum_{n=0}^{R_1-1} \overline{f}_{-r,-s}[n] q^*[n] = \frac{R_1}{RS} \delta_r \delta_s \tag{5.15}$$

$$0 \leq r \leq \overline{R} - 1, 0 \leq s \leq \overline{S} - 1$$

Here, δ_k denotes the Kronecker delta function, $\overline{f}_{r,s}[n] \triangleq f(n - rS)\overline{W}^{sn}$, and $\overline{W} = exp(\imath 2\pi \overline{S})$. Let $g[n]$, $f[n]$, and $q[n]$ be functions that repeat with a period of R_1. Solving the above expression for the computation of $q[n]$ and rewriting (5.15) as

$$\sum_{n=0}^{R_1-1} [f^*(n + rS)\overline{W}^{sn}] q[n] = \frac{R_1}{RS} \delta_r \delta_s \tag{5.16}$$

By applying the time shifting property of the DFT to equation (5.16), it can be obtained as

$$\sum_{n=0}^{R_1-1} q[n] \left[\frac{1}{R_1} \sum_{k=0}^{R_1-1} W^{rSk} F[k] W^{nk} \right]^* \overline{W}^{sn} = \frac{R_1}{RS}(1) \tag{5.17}$$

where $W = exp(\imath 2\pi / R_1)$. Further simplifying the aforementioned equation yields the following result

$$\frac{1}{R_1} \left[\sum_{n=0}^{R_1-1} q[n] W^{-nk} \right] \left[\sum_{k=0}^{R_1-1} F^*[k] W^{-rSk} \right] \overline{W}^{sn} = \frac{R_1}{RS} \tag{5.18}$$

$$\frac{1}{R_1} \left[Q(k) \right] \left[\sum_{k=0}^{R_1-1} F^*[k] W^{-rSk} \right] \overline{W}^{sn} = \frac{R_1}{RS} \tag{5.19}$$

The term $\overline{W}^{sn} = \exp(\imath 2\pi R_1 sn)$ equals one when the $R_1 sn$ has an integer value. Additionally, for $W^{-rSk} = \exp(-\imath 2\pi rSk/R_1)$ and $\sum_{k=0}^{R_1-1} \exp(-\imath 2\pi rSk/R_1) = R_1 \delta(k)$, the equation can

be further reduced to a simpler form as

$$Q(k)F^*[k] = \frac{R_1}{RS} \tag{5.20}$$

$$Q(k) = \frac{R_1}{(RS)F^*[k]} \tag{5.21}$$

Applying the Inverse Discrete Fourier Transform (IDFT) to both sides, the equation can be rewritten as

$$q[n] = \frac{R_1}{RS}\frac{1}{f^*[n]} \tag{5.22}$$

The equation in (5.22) characterizes the analysis window, denoted as $q[n]$. Based on (5.22), the expressions for both the synthesis window and the corresponding analysis window are obtained. The RRC window, employed as the synthesis window in this context, is given by

$$f[n] = \sum_{n=0}^{R_1-1}(0.2393)\text{sinc}\left(\frac{n}{R_1}\right)\frac{\cos(\pi\alpha n/R_1)}{(1-4\alpha^2n^2/{R_1}^2)} \tag{5.23}$$

and the corresponding analysis window can be calculated as

$$q[n] = \frac{(0.2393)R_1}{RS}\sum_{n=0}^{R_1-1}\frac{(1-4\alpha^2n^2/{R_1}^2)^*}{\text{sinc}(n/R_1)^*\cos(\pi\alpha n/R_1)^*} \tag{5.24}$$

The cross-Wigner distribution of $\hat{f}(n)$ and $\hat{q}(n)$ is given by [**?**]

$$\mathbf{W}_{\hat{f},\hat{q}}(p,l) = \frac{1}{2R_1}\sum_{n=0}^{R_1-1}\hat{f}(n)\hat{q}^*(p-n)\cdot\exp(-\frac{\iota\pi l}{R_1}(2n-p)) \tag{5.25}$$

where $\mathbf{W}_{\hat{f},\hat{q}}$ is a matrix sized $R_1 \times R_1$, facilitating a complete characterization of an arbitrary distribution function in the Wigner domain. By using this cross Wigner distribution, $\mathbf{W}^*_{\hat{f}_\alpha\hat{q}_\beta}(p,l)$ is calculated, which is a $R_1 \times R_1$ matrix and could be used as a basis in the mixed domain, enabling the expansion of any arbitrary time-frequency distribution [**?**]

$$\begin{aligned}\mathbf{W}^*_{\hat{f}_\alpha\hat{q}_\beta}(p,l) &= \mathbf{W}^*_{\hat{f}_{r,s}\hat{q}_{j,y}}(p,l)\\ &= exp\Big\{\iota\Big[\frac{\pi p}{S}(s-l)+\frac{\pi l}{R}(j-R)+\frac{2\pi\overline{S}}{S}(s-y)+\\ &\qquad\frac{\pi\overline{S}}{S}(s+y)(r+j)\Big]\Big\}\mathbf{W}_{\hat{f},\hat{q}}(p-(r+j)\overline{S},l-(s+y)\overline{R}),\end{aligned} \tag{5.26}$$

$$0 \le r,j \le R-1, \quad 0 \le s,y \le S-1$$

It is essential to observe that in this context, $\alpha \triangleq (r,s)$ and $\beta \triangleq (j,y)$ can represent both

two-dimensional indices, as well as any valid reordering into a one-dimensional index (such as $\hat{\alpha} = rS + s$ and $\hat{\beta} = jS + y$). The mixed domain basis is composed of basis functions that are each a shifted and modulated version of a fundamental basis function, thereby avoiding the requirement for repetitive computations. The corresponding expansion coefficients can be computed as [**?**]

$$\mathbf{C}_{\alpha,\beta} = 4R_1 \sum_{p=0}^{R_1-1} \sum_{l=0}^{R_1-1} \mathbf{Y}(p,l)\mathbf{W}^*_{\hat{q}_\alpha \hat{f}_\beta}(p,l) \tag{5.27}$$

where $\mathbf{Y}(p,l)$ is desired periodic function specified in the Wigner domain and is a matrix of $R_1 \times R_1$ dimension. The Gaussian window is considered as the desired periodic function. $\mathbf{C}_{\alpha,\beta}$ represents a matrix of $R\overline{S} \times R\overline{S}$. Error function ϵ can be minimized by choosing the maximum eigen vector corresponding to the largest positive eigen value λ_{max} of matrix $\mathbf{C}_{\alpha,\beta}$. This eigenvector, denoted as $\vec{E}max$ with dimensions $R_1 \times 1$, is subsequently normalized as

$$\tilde{\mathbf{E}}_{max} = [\lambda_{max}/(\vec{E}^T_{max}\mathbf{H}^T\mathbf{K}^*\vec{E}_{max})]^{1/2}\vec{E}_{max} \tag{5.28}$$

where

$$\mathbf{K} = \sum_{n=0}^{R-1} \hat{f}_\alpha[n]\hat{q}^*_\beta[n] \tag{5.29}$$

and

$$\mathbf{H} = \sum_{n=0}^{R-1} q_\beta[n]\hat{q}^*_\alpha[n] \tag{5.30}$$

and the matrix $\tilde{\mathbf{E}}_{max}$ gives the value of expansion coefficients $v_{r,s}$, hence substituting value of $v_{r,s}$ in (5.13)

$$g[n] = \sum_{r=0}^{R-1} \sum_{s=0}^{S-1} \tilde{\mathbf{E}}_{max}\hat{q}_{r,s}[n] \tag{5.31}$$

The calculated filter coefficients are used in GFDM transmitter and receiver. The method proposed for designing the pulse shaping filter is illustrated in Fig. 5.1, and the **Algorithm** outlining this proposed method is provided below.

Algorithm 1 Calculate $g[n]$

Require: $R, S, \overline{R}, \overline{S}, y[n]$ and $f[n]$.

Ensure: Oversampling case.

Step 1: Calculate corresponding analysis window $q[n]$ based on (5.22).

Step 2: Compute $\mathbf{W}_{\hat{f},\hat{q}}(p,l)$ and $\mathbf{W}^{*}_{\hat{f}_{\alpha}\hat{q}_{\beta}}(p,l)$ using (5.25) and (5.26).

Step 3: Compute $\mathbf{C}_{\alpha,\beta}$, $\mathbf{K}$ and $\mathbf{H}$ using (5.27), (5.29) and (5.30), respectively.

Step 4: Calculate the largest eigenvalue λ_{max} and corresponding eigenvector $\vec{E}_{max}$ of matrix $\mathbf{C}_{\alpha,\beta}$.

Step 5: Normalize $\vec{E}_{max}$ using (5.28)

Step 6: Evaluate $g[n]$ based on (5.31).

5.3 Performance Analysis

This section presents the performance analysis of GFDM system in terms of SER and PSD. A comparison is made between the results obtained with the proposed filter and those obtained with the conventional RRC filter, considering various values of the roll off factor. The ZF receiver is employed, as it effectively eliminates self-interference while also amplifying noise, a behavior influenced by the chosen pulse shape.

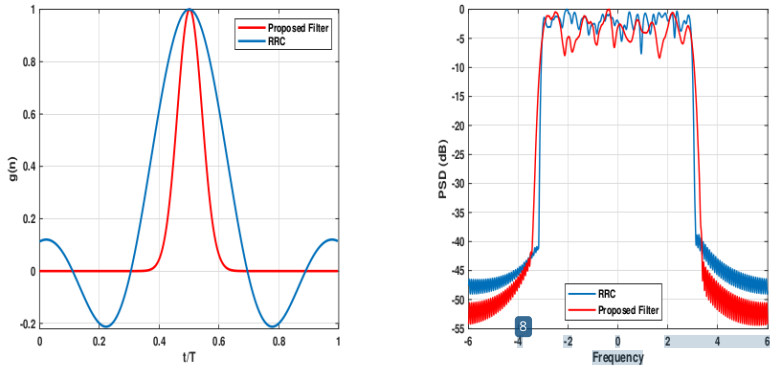

Figure 5.2: Time and frequency domain plots for RRC (α =0.1) and proposed (α =0.1) prototype filter

5.3.1 Power Spectral Density

The PSD represents the power content of a signal across different frequencies. The expression for PSD can be given as [**?**]

$$P(f) = \frac{1}{MT_s}\sum_{k,m}\left|G_m\left(f-\frac{k}{T_s}\right)\right|^2 \sum_{ukm} R_{ukm}e^{-j2\pi uMT_s f}$$
$$= \frac{1}{MT_s}\sum_{k,m}\left|G_m\left(f-\frac{k}{T_s}\right)\right|^2 \times S\left(f-\frac{k}{T_s}\right) \tag{5.32}$$

where, T_s represents the duration of a single sub-symbol, u denotes the block index within the range of $(\frac{-T}{2MT_s}, \frac{T}{2MT_s})$ while m and k encompass all the dedicated sub-symbols and sub-carriers. R_{ukm} denotes the auto correlation function of the information sequence $d_{u,m,k}$ and $S(f)$ represents the spectral content of the modulated data. G_m corresponds to the Fourier transform of $g_m[n]$. When data symbols are assumed to be i.i.d. with unit variance then the PSD expression can be reduced to [**?**]

$$P(f) = \frac{1}{MT_s}\sum_{k,m}\left|G_m\left(f-\frac{k}{T_s}\right)\right|^2, \tag{5.33}$$

The above equation makes it evident that the PSD of the GFDM system is influenced by selection of pulse shaping filter, and opting for an appropriate pulse shaping filter can effectively reduce OOB emissions. Figure 5.2 presents the impulse response $g[n]$ and PSD of the conventional RRC and proposed pulse shaping filters for the value of roll-off factor $\alpha = 0.1$. Furthermore, Figure 5.2 illustrates that proposed filter demonstrates higher side lobes, which play a role in improving the overall performance of GFDM system. Plot of PSD highlights that OOB emission for the proposed filter is notably reduced compared to the RRC filter.

5.3.2 Symbol Error Rate

This section provides numerical results of SER performance for the different fading channels. The simulation results are provided for M = 5 subsymbols, K = 64 subcarriers and a CP of 12. Table 5.1 provides the system parameter values utilized to evaluate the results. Results for proposed filter are presented in the case of the 4 & 16-QAM modulation scheme over diverse channels, that is AWGN, Rayleigh, Nakagami-m, TWDP, and Nakagami-q.

Now, ASER ($P(e)$) of the GFDM system in terms of γ is written as

$$P(e) = \int_0^\infty P(e/\gamma) f_\gamma(\gamma) d\gamma, \tag{5.34}$$

here, $f_\gamma(\gamma)$ is PDF of fading channel, and $P(e/\gamma)$ is the conditional ASER of the μ-QAM

modulation over AWGN which is given as [?]

$$P(e) = 2\left(\frac{t-1}{t}\right)\text{erfc}(\sqrt{\gamma}) - \left(\frac{t-1}{t}\right)(\text{erfc})^2(\sqrt{\gamma}) \tag{5.35}$$

here instantaneous SNR γ is given by

$$\gamma = \frac{3R_T}{2(2^\mu - 1)}\frac{E_s}{\xi N_o} \tag{5.36}$$

and

$$R_T = \frac{KM}{KM + N_{cp}} \tag{5.37}$$

where μ is the modulation order, $t = \sqrt{2^\mu}$, and N_{cp} represents the length of the CP. ξ stands for the noise enhancement factor (NEF), E_s denotes the average energy per symbol, and N_o represents noise power spectral density. Further, ξ can be defined in terms of receiver matrix **B** as

$$\xi = \sum_{n=0}^{N-1} |[\mathbf{B}]_{k,n}|^2, \tag{5.38}$$

The value of ξ is uniform for all values of k and for ZF receiver, **B** is inverse of transmitter matrix **A**. Now ξ can be obtained by substituting the value of **B** in (5.38) as

$$\xi = \sum_{n=0}^{N-1} |[\mathbf{A}^{-1}]_{k,n}|^2, \tag{5.39}$$

The factor γ is a crucial factor influencing the SER performance of GFDM. By substitute value of NEF from (5.39) in (5.36), the expression of γ can be computed as

$$\gamma = \frac{3R_T}{2(2^\mu - 1)} \frac{E_s}{\left[\sum_{n=0}^{N-1} |[\mathbf{A}^{-1}]_{k,n}|^2\right] N_o} \tag{5.40}$$

The expression of SER in (5.34) depends on γ, and (5.40) clearly depicts dependency of γ on NEF, which can be computed using a transmission matrix **A**. The entries of the transmission matrix **A** represent the pulse-shaping filter coefficients $g[n]$, shifted in both frequency and time, as defined in (5.4). The performance (SER) of GFDM is influenced directly by pulse shaping coefficients, which makes it a significant factor in the GFDM system.

Effective Gamma

Figure 5.3 presents a plot for effective γ verses SNR for 16-QAM scheme and a roll off factor of $\alpha = 0.7$. Figure depicts that effective γ is higher for proposed filter for all SNR values. A higher γ results in enhanced SER performance for GFDM. For instance, when using 16 QAM

modulation with a SNR of 10 dB and roll-off factor of $\alpha = 0.7$, the effective γ decreases from 1.4925 for proposed filter to 0.6280 for RRC filter. As the value of gamma decreases, the performance of GFDM system also degrades. The value of effective γ is determined by the value of NEF (ξ). For proposed filter NEF value is approximately half of the NEF value of RRC filter as shown in the following example. For the 16-QAM scheme and a constant roll-off factor of $\alpha = 0.5$, the NEF for RRC filter and the proposed filter is 1.2417 and 0.6411 respectively.

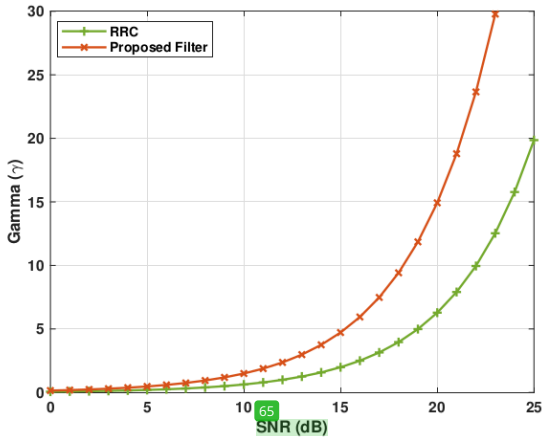

Figure 5.3: Plot for Effective γ and SNR for 16 QAM GFDM system at α = 0.7

AWGN Channel

The SER formulation for GFDM in an AWGN fading channel is given as [**?**]

$$P(e) = 2\left(\frac{t-1}{t}\right)\text{erfc}(\sqrt{\gamma}) - \left(\frac{t-1}{t}\right)(\text{erfc})^2(\sqrt{\gamma}) \tag{5.41}$$

here the value of γ is mentioned in (5.40). Figure 5.4 illustrates the relationship between SER and SNR for GFDM with 4 & 16 QAM modulation in presence of AWGN fading channel. The outcomes are demonstrated across two values of the roll-off factor (0.1 & 0.9), both for the conventional RRC filter and the proposed filter. When utilizing the proposed filter, the GFDM system's performance is significantly enhanced for $\alpha = 0.9$ compared to its performance at $\alpha = 0.1$.

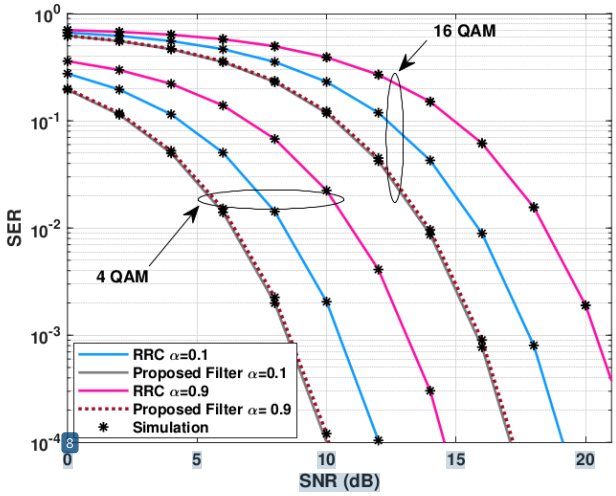

Figure 5.4: SER for 16 QAM GFDM system at $\alpha = 0.1$ & 0.9 under AWGN channel

Table 5.1: Simulation parameters for the GFDM.

Parameters	**Values**
Pulse Shaping Filter	RRC, Proposed
Roll off factor	0.1, 0.9
Modulation scheme	4,16 QAM
Number of subsymbols (M)	5
Number of subcarriers (K)	64
Length of CP (Ncp)	12
Receiver	Zero forcing (ZF)
Channel estimation	Perfect

Nakagami-m Fading Channel

The Nakagami-m model basically follows a central chi-square distribution where m is the Nakagami-m fading parameter, and the range of m is from $\frac{1}{2}$ to ∞. As m approaches $\frac{1}{2}$, the Nakagami-m fading channel converges to a one-sided Gaussian distribution. Similarly, as m approaches 1, it converges to a Rayleigh channel, and as m approaches $+\infty$, it converges to a nonfading AWGN channel [**?**]. The SER equation for the GFDM system under Nakagami-m

channel conditions is presented as follows [**?**]

$$P(e) = \frac{2}{\sqrt{\pi}}\left(\frac{\sqrt{c}}{(1+c)^{m+\frac{1}{2}}}\frac{\Gamma\left(m+\frac{1}{2}\right)}{\Gamma(m+1)}2I_1\left(1, m+\frac{1}{2}; m+1; \frac{1}{1+c}\right)\right.$$
$$\left. -\frac{2}{\sqrt{\pi}}\left(\frac{\sqrt{c}}{(1+c)^{2m+\frac{1}{2}}}\frac{\Gamma\left(2m+\frac{1}{2}\right)}{\Gamma(2m+1)}2I_1\left(1, 2m+\frac{1}{2}; 2m+1; \frac{1}{1+c}\right)\right.\right. \tag{5.42}$$

where

$$c = \frac{\beta\gamma}{m}$$

and

$$\beta = \frac{3R_T}{2(2^\mu - 1)}$$

Figure 5.5 presents the plot of SER vs E_s/N_o at $\alpha = 0.9$ for 16-QAM modulation scheme for the GFDM system over Nakagami-m channel for two values of fading parameter $m = 2$ and $m = 4$. It can be inferred that the SER performance improves for the larger value of fading parameter m. Compared to the conventional RRC filter, the proposed filter exhibits lower SER values, indicating that it outperforms the former.

Rayleigh Fading Channel

This section considers a time-varying Rayleigh fading channel, where the amplitude is a Rayleigh distribution, while the phase is uniformly distributed between π to positive π. The GFDM system's SER under Rayleigh fading model conditions is formulated as [**?**]

$$P(e) = 2\left(\frac{t-1}{t}\right)\left(1 - \sqrt{\frac{\gamma_r}{\gamma_r+1}}\right) - \left(\frac{t-1}{t}\right)^2$$
$$\times\left[1 - \frac{4}{\pi}\sqrt{\frac{\gamma_r}{\gamma_r+1}}\text{atan}\left(\sqrt{\frac{\gamma_r}{\gamma_r+1}}\right)\right] \tag{5.43}$$

where

$$\gamma_r = \frac{3\sigma_r^2 R_T}{(2^\mu - 1)}\frac{E_s}{\xi N_o} \tag{5.44}$$

Rayleigh Fading channel is a special case of Nakagami-m channel with $m = 1$. The performance of the GFDM system with 4 & 16-QAM modulation scheme under Rayleigh fading channel conditions for $\alpha = 0.1$ is depicted in Figure 5.6. The results clearly indicate that the proposed filter yields improved performance for 4 QAM compared to 16 QAM modulation

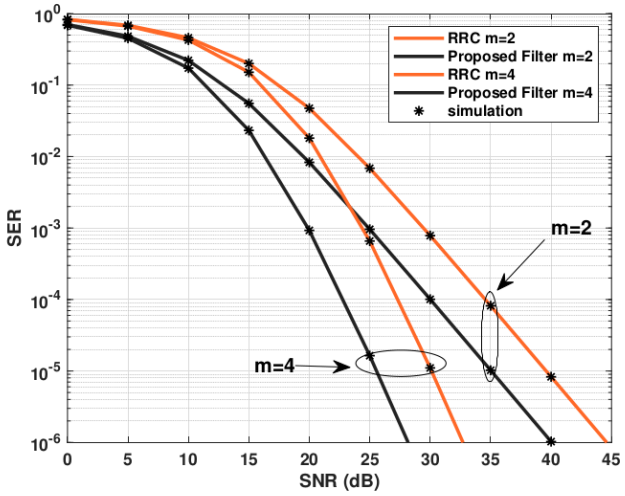

Figure 5.5: SER for 16 QAM GFDM system with $m = 2$ & 4 under Nakagami-m fading channel

scheme. The graph illustrates that proposed filter achieves better SER performance compared to the conventional RRC filter.

TWDP Fading Channel

In a TWDP fading channel, the received signal comprises of two relatively dominant multipath components along with several low-power diffuse components. K and Δ are two important channel parameters in the TWDP fading channel, here, K represents ratio between power of specular component to that of scattered component, and value of K varies from 0 to ∞. The parameter Δ denotes ratio of peak power to average power of the specular component and varies from 0 to 1. Rayleigh fading and Rician fading are two special cases of TWDP channel, when K is 0, it converts into Rayleigh fading, and when Δ becomes zero, it converts into Rician fading [**?**]. he SER formulation for GFDM under TWDP channel is given as [**?**]

$$P(e) = \frac{4}{\pi}\left(\frac{u-1}{u}\right)\left[\int_0^{\pi/2}\left[\frac{1+K}{1+K+c\gamma}exp\left(\frac{-Kc\gamma}{1+K+c\gamma}\right)I_o\left(\frac{-Kc\gamma\Delta}{1+K+c\gamma}\right)\right]d\theta - \frac{1}{\pi}\int_0^{\pi/2}\left[\frac{1+K}{1+K+c\gamma}exp\left(\frac{-Kc\gamma}{1+K+c\gamma}\right)I_0\left(\frac{-Kc\gamma\Delta}{1+K+c\gamma}\right)\right]\right]d\theta \tag{5.45}$$

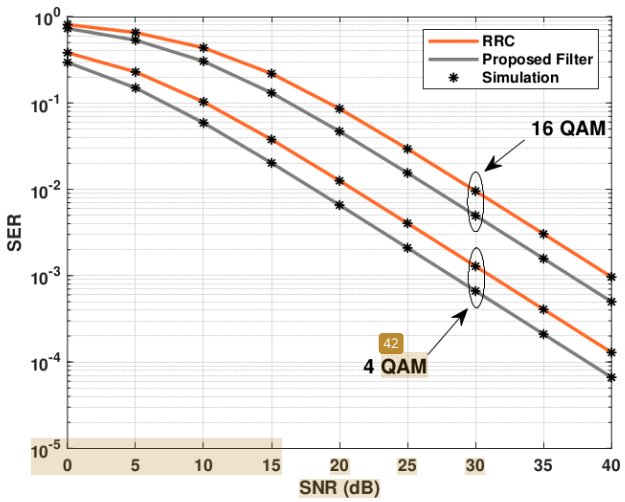

Figure 5.6: SER for 4 & 16 QAM GFDM system at $\alpha = 0.1$ under Rayleigh channel

where

$$c = \frac{-\beta}{sin^2\theta}$$

Figure 5.7 illustrates SER against SNR plot of the GFDM system under TWDP fading channel for 16-QAM modulation scheme for $\Delta = 0$ and various values of factor K. As the value of K varies from 0 to 10, the power of the specular components increases, resulting in an improvement in the performance of GFDM. Figure 5.7 depicts that SER performance improves for the proposed filter as compared to the conventional RRC filter.

Nakgami-q Fading Channel

The Nakagami-q fading model, also known as the Hoyt distribution, is characterized by the Nakagami-q fading parameter. This parameter, q, ranges from 0 to 1, where $q = 0$ represents one-sided Gaussian fading, and $q = 1$ corresponds to Rayleigh fading [**?**]. The expression of

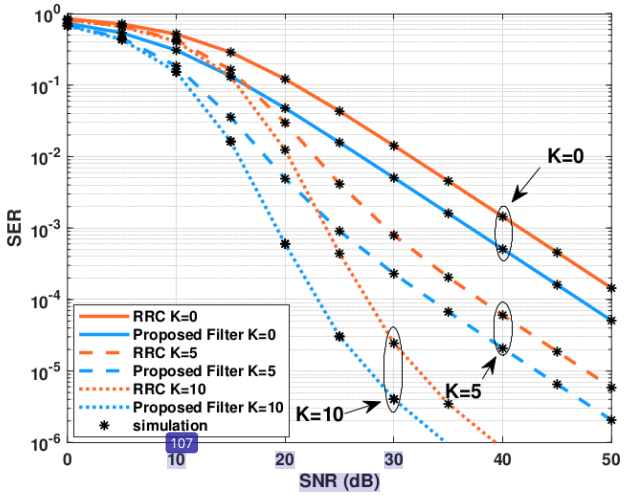

Figure 5.7: SER for 16 QAM GFDM system with $K = 0, 5, 10$ and $\Delta = 0$ under TWDP channel

SER for GFDM in the presence of a Nakagami-q channel is given by: [**?**]

$$P(e) = \frac{a}{\sqrt{\pi}} \frac{\Gamma\left(\frac{3}{2}\right)}{\Gamma(2)} M(c) F_D^{(2)}\left(\frac{1}{2}, \frac{1}{2}, \frac{1}{2}; 2; I_1, I_2\right) - \frac{a}{\pi^2(3)} M(2c) \\ F_D^{(3)}\left(\frac{1}{2}, \frac{1}{2}, \frac{1}{2}; 2; J_1, J_2\right), \tag{5.46}$$

where $F_D^{(n)}$ is Lauricella's hypergeometric function and values of M(c),I_1, I_2, J_1, J_2 are given as

$$M(c) = \left(\left(1 + c\frac{2\gamma}{(1+q^2)}\right)\left(1 + c\frac{2q^2\gamma}{(1+q^2)}\right)\right), \tag{5.47}$$

$$I_1 = \left(1 + \frac{2\gamma}{1+q^2}\right)^{-1}, I_2 = \left(1 + \frac{2q^2\gamma}{1+q^2}\right)^{-1},$$

and

$$J_1 = \frac{1 + \frac{2c\gamma}{1+q^2}}{1 + \frac{4c\gamma}{1+q^2}}, J_2 = \frac{1 + \frac{2q^2c\gamma}{1+q^2}}{1 + \frac{4q^2c\gamma}{1+q^2}}.$$

The graph in Figure 5.8 illustrates the SER against SNR for the GFDM with 16 QAM modula-

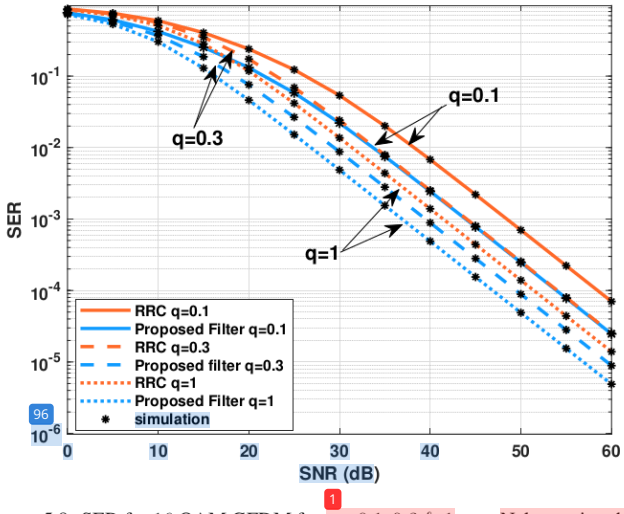

Figure 5.8: SER for 16 QAM GFDM for $q = 0.1, 0.3$ & 1 over Nakagami-q channel

tion scheme, at $\alpha = 0.9$, operating under Nakagami-q fading channel conditions with q values of 0.1, 0.3, and 1. As illustrated in Figure 5.8, the GFDM performance for the proposed filter exhibits improvement as the parameter q increases. This enhancement is due to the increased power of specular components, leading to improved SER performance, with the optimal performance observed at $q = 1$.

5.4 Summary

This chapter introduces a novel filter design method using discrete biorthogonality condition. The filter coefficients are calculated using discrete Gabor representation, and these coefficients are subsequently used in the GFDM system. The proposed filter's performance is numerically analyzed through Monte Carlo simulations across diverse fading channels, including AWGN, Rayleigh, Nakagami-m, TWDP, and Nakagami-q.

Chapter 6

Conclusion and Future Scope

This chapter summarizes the conclusions drawn from the analytical and simulation studies conducted throughout this dissertation. The research primarily focused on enhancing the performance of GFDM-based 5G communication systems. To achieve this, the performance of GFDM was analyzed and then improved by proposing new synchronization techniques and a pulse shaping filter.

6.1 Conclusion

Chapter 1 provides a brief introduction to the $5G$ communication system, highlighting its requirements, applications, and key technologies. Additionally, the chapter discusses the necessity and applications of the GFDM system. Chapter 2 outlines the GFDM system model and provides an extensive review of the latest research advancements made by various scholars in the field of GFDM.

Chapter 3 analyzes performance of GFDM using the ASER as a performance metric for the FTR fading channel. The chapter discusses various performance analysis metrics and the characteristics of the FTR fading channel. An exact closed-form formula for ASER is obtained for GFDM systems operating over the FTR fading channel, taking into account imperfect channel estimation. Furthermore, an asymptotic analysis is conducted to gain deeper insights into performance of GFDM.

Chapter 4 introduces a novel timing synchronization algorithm for estimating the timing offset in GFDM systems, employing a chirp signal as a training symbol. Chapter 5 focuses on the design of pulse-shaping filter for GFDM, utilizing discrete Gabor representation, biorthogonality conditions, and WD. Additionally, performance of the GFDM system is analyzed across various fading channels.

The main contributions of this dissertation are summarized as:

- Derived close form expression of ASER of GFDM system over FTR fading channel
- ASER performance of GFDM

- Effect of imperfect CSI on instantaneous SNR and ASER
- Proposed new synchronization technique
- Proposed new pulse shaping filter
- Comparison of simulations and analytical results

6.2 Future Work

This dissertation focuses on enhancing GFDM-based $5G$ communication systems by analyzing performance of the GFDM over mmWave channels, particularly for FTR channel. To further improve system performance, a new synchronization technique and a pulse-shaping filter are proposed. While $5G$ is still in its early stages of deployment and expansion, researchers and industry experts are already exploring the requirements, challenges, and opportunities for "beyond $5G$" (B5G) communication. As the global community aims to redefine future wireless communication systems, the development of $B5G$ is gaining significant attention. Despite the comprehensive research presented in this dissertation, there remains ample scope for further investigation. Some key areas that require additional study include:

- The proposed synchronization technique and pulse-shaping filter can be adapted for use with other waveforms and systems, including NOMA, FBMC, UFMC, and OTFS.
- The effectiveness of the proposed algorithms can be assessed across various fading channels and potentially applied in future $6G$ wireless communication systems.
- The GFDM system's performance can be evaluated using channels that effectively represent the characteristics of modern wireless communication systems.

Manpreet Thesis

ORIGINALITY REPORT

13%	8%	10%	2%
SIMILARITY INDEX	INTERNET SOURCES	PUBLICATIONS	STUDENT PAPERS

PRIMARY SOURCES

1	Surbhi Kalsotra, Ashutosh Kumar Singh, Hem Dutt Joshi. "Performance analysis of space time coded generalized frequency division multiplexing system over generalized fading channels", Transactions on Emerging Telecommunications Technologies, 2021 Publication	1%
2	hdl.handle.net Internet Source	1%
3	mafiadoc.com Internet Source	<1%
4	Submitted to University of Surrey Student Paper	<1%
5	Marvin K. Simon, Mohamed-Slim Alouini. "Digital Communication over Fading Channels", Wiley, 2004 Publication	<1%
6	Yashpreet Kaushal, Hem Dutt Joshi, Ashutosh Kumar Singh, Amit Mishra, Bhaskar Gupta. "Zadoff–Chu Sequence Based Timing Offset Estimation for OFDM Systems", Wireless Personal Communications, 2017 Publication	<1%
7	Mona Devi Laishram, Dinamani Singh Aheibam. "Performance of dual-branch selection combining receiver over Fluctuating Two-Ray (FTR) fading channels for 5G	<1%

	mmWave communications", AEU - International Journal of Electronics and Communications, 2020 Publication	
8	dokumen.pub Internet Source	<1%
9	unidel.edu.ng Internet Source	<1%
10	tudr.thapar.edu:8080 Internet Source	<1%
11	worldwidescience.org Internet Source	<1%
12	"Communications, Signal Processing, and Systems", Springer Science and Business Media LLC, 2020 Publication	<1%
13	Muntadher Alsabah, Marwah Abdulrazzaq Naser, Basheera M. Mahmmod, Sadiq H. Abdulhussain et al. "6G Wireless Communications Networks: A Comprehensive Survey", IEEE Access, 2021 Publication	<1%
14	Nicola Michailow, Maximilian Matthe, Ivan Simoes Gaspar, Ainoa Navarro Caldevilla et al. "Generalized Frequency Division Multiplexing for 5th Generation Cellular Networks", IEEE Transactions on Communications, 2014 Publication	<1%
15	arxiv.org Internet Source	<1%
16	wsl.stanford.edu Internet Source	<1%
	Submitted to University of Queensland	

17	Student Paper	<1%
18	core.ac.uk Internet Source	<1%
19	link.springer.com Internet Source	<1%
20	"OFDM and alternative waveforms", Institution of Engineering and Technology (IET), 2020 Publication	<1%
21	Abhijit Bhowmick, Yogesh Kumar Choukiker, Indrasen Singh, Arumugam Nallanathan. "5G and Beyond Wireless Communications - Fundamentals, Applications, and Challenges", CRC Press, 2024 Publication	<1%
22	Shravan Kumar Bandari, Venkata Mani Vakamulla, Anastasios Drosopoulos. "GFDM/OQAM performance analysis under Nakagami fading channels", Physical Communication, 2018 Publication	<1%
23	www.mdpi.com Internet Source	<1%
24	Submitted to Asia Pacific University College of Technology and Innovation (UCTI) Student Paper	<1%
25	Hongxin Lin, Cheng Zhang, Yongming Huang, Rui Zhao, Luxi Yang. "Performance of Remote Radio Unit Selection in Millimeter Wave Distributed Antenna Systems over Fluctuating Two-Ray Fading", IEEE Wireless Communications Letters, 2021 Publication	<1%

26	Sandeep Shukla, Vijay Shanker Tripathi. "Performance Evaluation of Timing Estimation Technique Using Extended Cyclic Prefix for Correlation Sequence for OFDM Systems", Wireless Personal Communications, 2017 Publication	<1 %
27	Navuday Sharma, Atul Kumar, Haris Pervaiz, Maurizio Magarini et al. "Aerial Base Station Assisted Cellular Communication: Performance and Trade-Off", IEEE Transactions on Network Science and Engineering, 2021 Publication	<1 %
28	edoc.site Internet Source	<1 %
29	www.arxiv-vanity.com Internet Source	<1 %
30	www.politesi.polimi.it Internet Source	<1 %
31	ynu.repo.nii.ac.jp Internet Source	<1 %
32	Ayhan Yenilmez, Tansal Gucluoglu, Piotr Remlein. "Performance of GFDM-maximal ratio transmission over Nakagami-m fading channels", 2016 International Symposium on Wireless Communication Systems (ISWCS), 2016 Publication	<1 %
33	"Towards 5G", Wiley, 2016 Publication	<1 %
34	Vidhyacharan Bhaskar, Nagireddy Peram. "Performance modeling of finite state Markov chains for Nakagami-q and α–μ distributions	<1 %

over adaptive modulation and coding schemes", AEU - International Journal of Electronics and Communications, 2013
Publication

35	epdf.tips Internet Source	<1%
36	Andrea Paci, Matteo Chiacchia, Giuseppe Bianchi. "5GMap: Enabling external audits of access security and attach procedures in real-world cellular deployments", Computer Communications, 2025 Publication	<1%
37	Submitted to Thapar University, Patiala Student Paper	<1%
38	Waleed Alghrairi, Nasri Sulaiman, Maryam M. Isa, Ratna K. Z. Sahbudin, Siti Lailatul M. Hassan, Emad Hmood Salman. "A 5G Waveforms Detection based-Windowed Cosine-Hamming Filter", 2021 International Conference on Advance of Sustainable Engineering and its Application (ICASEA), 2021 Publication	<1%
39	ir.library.oregonstate.edu Internet Source	<1%
40	Megha Gupta, R. S. Gamad. "Symbol Error Rate Analysis of Generalized Frequency Division Multiplexing in Pulse Shaping Root Raised Cosine Filter", 2022 IEEE 11th International Conference on Communication Systems and Network Technologies (CSNT), 2022 Publication	<1%
41	Submitted to University of Birmingham Student Paper	<1%

42	hal.archives-ouvertes.fr Internet Source	<1%
43	Daljeet Singh, Hem Dutt Joshi. "Performance analysis of SFBC-OFDM system with channel estimation error over generalized fading channels", Transactions on Emerging Telecommunications Technologies, 2018 Publication	<1%
44	Arun Kumar, Nishant Gaur, Aziz Nanthaamornphong. "Signal detection of M-MIMO-orthogonal time frequency space modulation using hybrid algorithms: ZFE + MMSE and ZFE + MF", Results in Engineering, 2024 Publication	<1%
45	espace.inrs.ca Internet Source	<1%
46	Maurice Odida. "Network Slicing in Software DefinedNetworking for 5G", Research Square Platform LLC, 2024 Publication	<1%
47	Mingxin Liu, Wei Xue, Jincheng Gao, Peisong Jia, Yidong Xu, Sergey V. Volvenko. "Prototype Filter Design for Effectively Suppressing Out-of-Band Radiation in GFDM Systems", IEEE Communications Letters, 2023 Publication	<1%
48	Telagathoti Pitchaiah, Ravi Sekhar Yarrabothu. "Performance analysis of OQAM based GFDM 5G systems under line of sight fading scenarios", 2017 International Conference on Intelligent Sustainable Systems (ICISS), 2017 Publication	<1%

49	Ijiga, Owoicho Emmanuel. "Channel Estimation Techniques for Filter Bank Multicarrier Based Transceivers for Next Generation of Wireless Networks", University of the Witwatersrand, Johannesburg (South Africa), 2025 Publication	<1%
50	Qingyu Zhu, Zhiqiang Liu. "Constant-modulus Preamble Design for MIMO-OFDM Systems", 2006 IEEE International Conference on Acoustics Speed and Signal Processing Proceedings, 2006 Publication	<1%
51	Shravan Kumar Bandari, Venkata Mani Vakamulla, Anastasios Drosopoulos. "PAPR analysis of wavelet based multitaper GFDM system", AEU - International Journal of Electronics and Communications, 2017 Publication	<1%
52	Yu-Kuan Chang, Fang-Biau Ueng, Kun-Zhan Wu. "A novel MIMO-GFDM receiver for next generation communication", Transactions on Emerging Telecommunications Technologies, 2018 Publication	<1%
53	Mohammad Asif Habibi, Meysam Nasimi, Bin Han, Hans D. Schotten. "A Comprehensive Survey of RAN Architectures Toward 5G Mobile Communication System", IEEE Access, 2019 Publication	<1%
54	prism.ucalgary.ca Internet Source	<1%
55	publications.polymtl.ca	

	Internet Source	<1%
56	rucore.libraries.rutgers.edu Internet Source	<1%
57	www.coursehero.com Internet Source	<1%
58	Byungju Lim, Young-Chai Ko. "SIR Analysis of OFDM and GFDM Waveforms With Timing Offset, CFO, and Phase Noise", IEEE Transactions on Wireless Communications, 2017 Publication	<1%
59	Kostas P. Peppas, Anastasios Skrivanos, Evangelos Xenos, Jiayi Zhang, Ioannis Kouretas, Spyridon Chronopoulos. "Effective Capacity of Fluctuating Two-Ray Channels with Arbitrary Fading Parameters", 2018 IEEE 19th International Workshop on Signal Processing Advances in Wireless Communications (SPAWC), 2018 Publication	<1%
60	Miguel Lopez-Benitez, Ogeen H. Toma, Dhaval K. Patel, Kenta Umebayashi. "Sample Size Analysis of Energy Detection under Fading Channels", 2020 IEEE Wireless Communications and Networking Conference Workshops (WCNCW), 2020 Publication	<1%
61	dr.ntu.edu.sg Internet Source	<1%
62	ebin.pub Internet Source	<1%
63	eprints.soton.ac.uk Internet Source	<1%

64	file.scirp.org Internet Source	<1%
65	researchspace.ukzn.ac.za Internet Source	<1%
66	Adamu, Paul Ushiki. "Multi-Connectivity Techniques for Improved Performance in Mobile Communications", The University of Liverpool (United Kingdom), 2024 Publication	<1%
67	Yawgeng A. Chau. "Switching rate and receiver performance of binary modulations with the selection-and-stay combining over independent and correlated Nakagami-m fading channels", International Journal of Communication Systems, 2011 Publication	<1%
68	www.docstoc.com Internet Source	<1%
69	Submitted to Eastern Michigan University Student Paper	<1%
70	Jun Xu, Junmei Yao, Lu Wang, Kaishun Wu, Lei Chen, Wei Lou. "Revolution of Self-Organizing Network for 5G MmWave Small Cell Management: From Reactive to Proactive", IEEE Wireless Communications, 2018 Publication	<1%
71	Submitted to Pacific University Student Paper	<1%
72	Submitted to University of Bristol Student Paper	<1%
73	patents.google.com Internet Source	<1%

74	dx.doi.org Internet Source	<1%
75	thesis.library.caltech.edu Internet Source	<1%
76	Submitted to City University of Hong Kong Student Paper	<1%
77	Julius Ssimbwa, Byungju Lim, Young-Chai Ko. "GFDM frame design for low-latency industrial networks", Journal of Communications and Networks, 2022 Publication	<1%
78	Rami van der Molen. "An Analytical Concordance of the Verb, the Negation and the Syntax in Egyptian Coffin Texts (2 vols)", Brill, 2005 Publication	<1%
79	eprints.qut.edu.au Internet Source	<1%
80	etd.lib.metu.edu.tr Internet Source	<1%
81	www.digchip.com Internet Source	<1%
82	dlibrary.univ-boumerdes.dz:8080 Internet Source	<1%
83	manualzz.com Internet Source	<1%
84	patents.justia.com Internet Source	<1%
85	uzspace.unizulu.ac.za Internet Source	<1%
86	www.researchgate.net Internet Source	

		<1%
87	www.telecomtrainer.com Internet Source	<1%
88	zeidler.ucsd.edu Internet Source	<1%
89	A-lin Yongwiriyakul, Watcharapan Suwansantisuk. "Time and Frequency Synchronization of GFDM Waveforms for IoT Applications", 2020 59th Annual Conference of the Society of Instrument and Control Engineers of Japan (SICE), 2020 Publication	<1%
90	Ersin Öztürk, Ertugrul Basar, Hakan Ali Çırpan. "Multiple-input multiple-output generalized frequency division multiplexing with index modulation", Physical Communication, 2019 Publication	<1%
91	Hussein T. Mouftah, Melike Erol-Kantarci, Sameh Sorour. "Connected and Autonomous Vehicles in Smart Cities", CRC Press, 2020 Publication	<1%
92	S.L. Miller. "Acquisition performance in transmission diversity CDMA systems", GLOBECOM 01 IEEE Global Telecommunications Conference (Cat No 01CH37270) GLOCOM-01, 2001 Publication	<1%
93	Sairam Vamsi Tadikamalla, Harish Chandra Mohanta, Sudheer Kumar Terlapu, Vamshi Krishna Mandhapati. "Enhanced pulse shaping filters for minimizing interference in GFDM signals for 5G cellular networks",	<1%

	International Journal of Informatics and Communication Technology (IJ-ICT), 2025 Publication	
94	d.researchbib.com Internet Source	<1%
95	espace.etsmtl.ca Internet Source	<1%
96	sun.ti.rwth-aachen.de Internet Source	<1%
97	"High-Performance Modelling and Simulation for Big Data Applications", Springer Science and Business Media LLC, 2019 Publication	<1%
98	"Orthogonal Frequency Division Multiplexing for Wireless Communications", Springer Nature, 2006 Publication	<1%
99	Divyanshu Pandey, Harry Leib. "The Tensor Multi-Linear Channel and Its Shannon Capacity", IEEE Access, 2022 Publication	<1%
100	Joarder Jafor Sadique, Shaikh Enayet Ullah, Raad Raad, Md. Rabiul Islam et al. "Gyre Precoding and T-Transformation-Based GFDM System for UAV-Aided mMTC Network", Electronics, 2021 Publication	<1%
101	L. M. Barba-Maza, G. Jovanovic Dolecek. "PAPR reduction of GFDM system using Xia pulse and OPTS scheme", 2020 IEEE 63rd International Midwest Symposium on Circuits and Systems (MWSCAS), 2020 Publication	<1%

102	Myonghee Park, Namshin Cho, Jaehee Cho, Daesik Hong. "Robust integer frequency offset estimator with ambiguity of symbol timing offset for OFDM systems", Proceedings IEEE 56th Vehicular Technology Conference, 2002 Publication	<1 %
103	Sha, Yi, MingMing Li, and Jiafu Chu. "A novel Timing and Frequency Synchronization Technology for OFDM System", Journal of Networks, 2011. Publication	<1 %
104	Valluri Siva Prasad, Venkata Mani Vakamulla, Chakravarthy Gunturu. "Implementation of GFDM System Using USRP", Wireless Personal Communications, 2024 Publication	<1 %
105	jyx.jyu.fi Internet Source	<1 %
106	kclpure.kcl.ac.uk Internet Source	<1 %
107	lirias.kuleuven.be Internet Source	<1 %
108	oa.upm.es Internet Source	<1 %
109	patentimages.storage.googleapis.com Internet Source	<1 %
110	static.tongtianta.site Internet Source	<1 %
111	warwick.ac.uk Internet Source	<1 %
112	www.cse.iitb.ac.in Internet Source	

		<1%
113	www.freepatentsonline.com Internet Source	<1%
114	www.kingtoptec.com Internet Source	<1%
115	ytd2525.wordpress.com Internet Source	<1%
116	"Modelling and Simulation of Diffusive Processes", Springer Science and Business Media LLC, 2014 Publication	<1%
117	Andrei N Borodin. "Stochastic Processes", Springer Science and Business Media LLC, 2017 Publication	<1%
118	Behzad Mozaffari Tazehkand, Mohammad Reza Ghavidel Aghdam, Reza Abdolee, Aysan Kamyab. "Optimal prototype filter design in GFDM systems for self-interference elimination: A novel signal processing approach", Signal Processing, 2025 Publication	<1%
119	Enes, Ricardo. "Hybrid Iterative Equalizer for Massive MIMO Millimeter Wave CE-OFDM Systems", Universidade de Aveiro (Portugal), 2024 Publication	<1%
120	Fei Hu. "Opportunities in 5G Networks - A Research and Development Perspective", CRC Press, 2019 Publication	<1%

121	Iyad Falujah. "", IEEE Transactions on Wireless Communications, 4/2008 Publication	<1%
122	Li, Shuangyang. "Orthogonal Time Frequency Space (OTFS) Modulation for Wireless Communications.", University of New South Wales (Australia) Publication	<1%
123	Nan Tang, Shiwen He, Chunlin Xue, Yongming Huang, Luxi Yang. "IQ Imbalance Compensation for Generalized Frequency Division Multiplexing Systems", IEEE Wireless Communications Letters, 2017 Publication	<1%
124	Sulaiman Saleem Patel, Tahmid Quazi, Hongjun Xu. "Error performance of Uncoded Space Time Labelling Diversity in spatially correlated Nakagami-q channels", International Journal of Communication Systems, 2018 Publication	<1%
125	Surbhi Kalsotra, Atul Kumar, Hem Dutt Joshi, Ashutosh Kumar Singh, Kapal Dev, Maurizio Magarini. "Impact of Pulse Shaping Design on OOB Emission and Error Probability of GFDM", 2019 IEEE 2nd 5G World Forum (5GWF), 2019 Publication	<1%
126	Taesang Yoo. "", IEEE Transactions on Information Theory, 5/2006 Publication	<1%
127	ir.nctu.edu.tw Internet Source	<1%
	iris.polito.it	

128	Internet Source	<1%
129	isr.umd.edu Internet Source	<1%
130	repository.kaust.edu.sa Internet Source	<1%
131	scholar.lib.vt.edu Internet Source	<1%
132	silo.pub Internet Source	<1%
133	techneconomyblog.com Internet Source	<1%
134	vdoc.pub Internet Source	<1%
135	web.mitsgwalior.in Internet Source	<1%
136	www.gssrr.org Internet Source	<1%
137	www.labunix.uqam.ca Internet Source	<1%
138	www.trademarkelite.com Internet Source	<1%

Exclude quotes	Off	Exclude matches	< 8 words
Exclude bibliography	On		